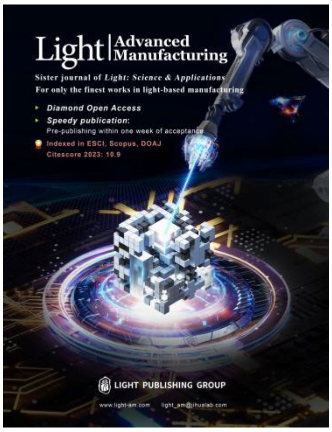

Polarization Optical Metrology for Linear Birefringence in Transparent Anisotropic Medium

Shiwei Deng, Xunda Chang, Kerong Jiao, Kewu Li, Xin Xu, Yifan Wang, Jiayu Wang, Hua Shen and Yidong Tan

Cite this article as: Shiwei Deng, Xunda Chang, Kerong Jiao, Kewu Li, Xin Xu, Yifan Wang, Jiayu Wang, Hua Shen and Yidong Tan. Polarization Optical Metrology for Linear Birefringence in Transparent Anisotropic Medium. *Light: Advanced Manufacturing* accepted article preview 29 April 2026; doi: 10.37188/lam.2026.078

Received 5 September 2025; revised 28 April 2026; accepted 28 April 2026;
Accepted article preview online 29 April 2026

Polarization Optical Metrology for Linear Birefringence in Transparent Anisotropic Medium

Shiwei Deng[1,2,3], Xunda Chang[1], Kerong Jiao[3], Kewu Li[2], Xin Xu[1], Yifan Wang[1], Jiayu Wang[2], Hua Shen[3,*] Yidong Tan[1,*]

[1] State Key Laboratory of Precision Measurement Technology and Instruments, Department of Precision Instrument, Tsinghua University, Beijing, 100084, China.

[2] State key Laboratory of Extreme Environment Optoelectronic Dynamic Measurement Technology and Instrument, North University of China, Tai Yuan, 030051, China.

[3] MIIT Key Laboratory of Advanced Solid Laser, Nanjing University of Science and Technology, Nanjing 210094, China.

*edward_bayun@163.com

*tanyd@tsinghua.edu.cn

Abstract

Birefringence refers to the optical anisotropy of transparent media, manifesting as light-wave splitting and phase differences owing to the direction-dependent refractive indices. This phenomenon is closely related to the internal microstructure, stress state, and external fields that affect materials. In recent years, birefringence analysis has gained increasing attention as a powerful tool for revealing the microscopic anisotropic features, polarisation responses, and macroscopic stresses that are difficult to observe using conventional methods. The accurate measurement and characterisation of birefringence in transparent media have become critical in fields such as materials science, biomedicine, and precision manufacturing. This paper provides a comprehensive review of the methods used for birefringence measurement based on polarisation optics. First, it introduces the birefringent polarisation optical theory, mechanisms of birefringence, and classification of the measurement characteristics. Subsequently, common techniques including polarisation modulation analysis, interferometric methods, and other optical approaches are presented in detail, covering their principles, features, advantages, limitations, and applicable scenarios. Recent research advances are also discussed, with an emphasis on applications such as residual stress analysis, characterisation of advanced material anisotropy, pathological diagnosis in biological tissues, and performance evaluation of novel birefringent components. Finally, current challenges are outlined, and future trends in the field are proposed.

Keywords: Birefringence; Phase retardance; Polarization optics; Optical interference; Anisotropic media

Introduction

In the 17th century, Danish scientist Bartholin noted the peculiar image-doubling phenomenon in calcite, marking the first record of birefringence. Birefringence fundamentally arises from the orderly internal arrangement of transparent media and is manifested as anisotropic refractive indices in different directions[1]. In anisotropic media, orthogonal polarisation components have different refractive indices, leading to beam splitting and optical path differences[2]. Here, the refractive index depends not only on the wavelength and the material itself but also on the propagation direction and polarization orientation[3]. In particular, the polarisation eigenstates of light manifest as two mutually orthogonal linear polarisation states with linear birefringence. Ordinary light follows the classical Snell's law, whereas extraordinary light requires solving Snell's law together with the refractive-index ellipsoid equation to determine the actual direction of its wave vector and effective refractive index[4, 5]. In modern photonics and engineering, birefringence not only possesses profound physical significance, but also serves as an indispensable parameter for polarisation control and sensing in engineering applications, forming the foundation of polarization optics[6]. On the one hand, by artificially controlling the birefringence properties of materials, it is possible to actively and precisely manipulate the propagation path and polarization state of light, enabling broad applications in metasurface-based wavefront and polarization control[7], optical communication[8], advanced display technologies[9], as well as photonic and optical instrumentation systems[10]. On the other hand, the intrinsic birefringence of materials can passively and intuitively reveal their internal structures and characteristics, offering powerful analytical tools for materials science[11], biomedical sciences[12], and advanced optical detection techniques.

In recent years, transparent media[13] as core components of high-end optical systems in fields ranging from large scientific instruments to micro-precision platforms have seen a continuously growing demand for birefringence analysis and measurement[13, 14]. This trend stems from the unique capability of birefringence to reveal optical anisotropy, stress distribution, and microscopic structural orientation within materials. By measuring the birefringence, subtle internal details that are otherwise inaccessible through conventional methods can be determined. Transparent media, such as glass, crystals, polymer films, and biological tissues, often exhibit slight but physically meaningful birefringence effects under processing, operational conditions, or external fields, reflecting internal structural states and stress variations[15]. With the advances in optical manufacturing, micro/nanophotonics, and biomedical imaging technologies, there is an increasing demand for high-sensitivity, high-resolution birefringence measurement techniques. For instance, birefringence is used in fabrication to assess stress nonuniformity[15]. In the biomedical field, birefringence in tissue sections or live samples is used to identify collagen fibre orientation and detect tumour architecture, thereby providing label-free, high-contrast imaging[16]. Furthermore, the emergence of functional materials[17], such as two-dimensional materials, anisotropic metamaterials, and strain-tunable media, has introduced complex polarisation responses, making birefringence characterisation an essential tool for material development and performance evaluation. Therefore, the accurate measurement of birefringence parameters is crucial for investigating internal structures of materials, designing advanced polarisation optical devices, analysing component stress and defects, and imaging biological tissues.

The polarisation state of light directly reflects the birefringence characteristics of a material, prompting extensive research on optical polarisation methods[18]. Compared to traditional techniques such as mechanical testing, electron microscopy, and X-ray diffraction, polarisation-based methods, which leverage the sensitivity of the polarisation state to differences in refractive indices, enable non-contact, non-destructive, and quantitative measurements with superior sensitivity, spatial resolution, and real-time imaging[19, 20]. In this review, recent advances in birefringence measurement techniques based on polarisation for transparent media are systematically surveyed, providing a comprehensive analysis of their physical basis, technical implementations, and representative applications, as illustrated in Fig. 1. This review begins by presenting the fundamental types of birefringence—natural, engineered, and field-induced—and then classifying representative materials according to their characteristic birefringence parameters. Building on a unified Jones–Mueller formalism and the corresponding method-specific measurement mechanisms, this review emphasises polarimetric modulation analysis methods, interferometric measurement approaches, and other polarisation measurement techniques. In the modulation analysis category, the performance parameters, modulation strategies, and application adaptabilities of various modulators are compared. Within the interferometric methods, the optical configurations and technical features of different interferometers are systematically analysed and contrasted. In addition to these mainstream approaches, measurement principles and characteristics of alternative methods are discussed. The application section summarises the practical implementation of birefringence measurement techniques in fields, such as stress analysis, material characterisation, biological tissue imaging, and optical component calibration. A comparative table outlines the advantages and limitations of the different measurement methods in terms of accuracy, system complexity, and applicable range. Finally, the review concludes with a discussion on the current technical challenges and future development directions. This review aims to provide a clear, comprehensive, and balanced technical reference for researchers in the field of polarisation optical measurements and to guide future innovations in birefringence metrology.

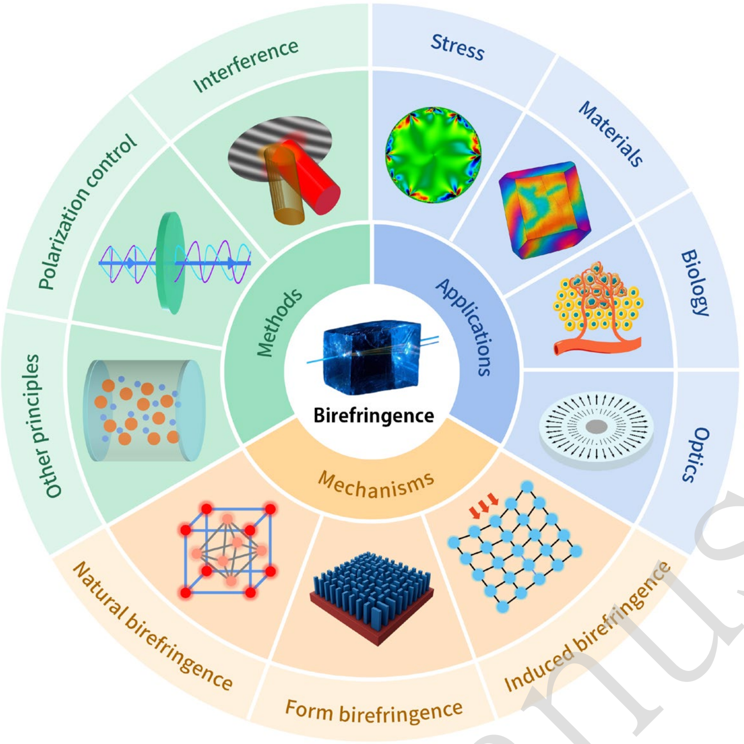

Fig. 1. Overview of mechanisms, methods, and applications of linear birefringence.

Fundamentals of Birefringence

The anisotropy of molecular arrangements in transparent media causes different polarisation propagations with different refractive indices, fundamentally causing birefringence. According to electromagnetic and crystal-optical theories, birefringence arises from the anisotropy of the refractive index tensor of the medium, represented by index ellipsoids with unequal axes[21]. The index ellipsoid visually depicts how the refractive index of a crystal varies with beam direction and polarisation state. The length of the semi-axis of the ellipsoid in a given direction represents the refractive index in that direction[22]. In isotropic materials, the refractive-index ellipsoid degenerates into a sphere (Fig. 2a), yielding only one refracted beam that follows Snell's law. Anisotropic crystals have two ellipsoids corresponding to the orthogonal ordinary (o) and extraordinary (e) waves. There can be one or two special directions in anisotropic crystals called optical axes, along which light does not experience birefringence. When light enters in any direction (Fig. 2b), it splits into o- and e-waves with different indices and velocities, which refract separately and produce birefringence.

Along the optical axis (Fig. 2b), the ordinary and extraordinary refractive indices become identical, therefore the medium behaves isotropically. However, perpendicular non-axial incidence (Fig. 2c) yields same-direction refraction with a phase shift. This phenomenon is widely applied to active or passive control of light polarisation. This review focuses on measuring the birefringence in such samples, characterised by two equally important parameters: phase retardance, which determines the phase difference introduced between the two polarisation components, and retardance axis orientation (fast or slow), which determines the direction of polarisation decomposition.

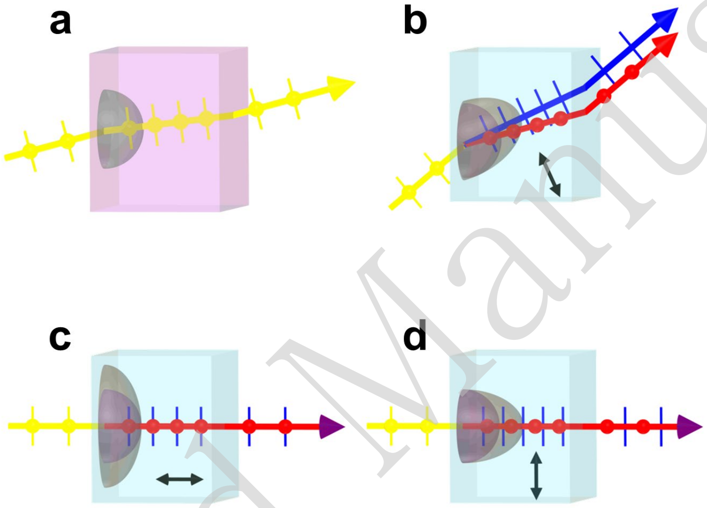

Fig. 2. Illustration of birefringence. Light propagates in an isotropic crystal (a) and positive uniaxial anisotropic crystal with different incident directions (b)-(d). (b) Incident from an arbitrary/general direction. (c) Incident along the optical axis. (d) Incident perpendicular to the optical axis.

Mechanism of birefringence

The mechanisms responsible for birefringence can be classified as natural, engineered, and induced. Natural birefringence[23] stems from the intrinsic anisotropy of the crystal structure of the material, that is, the asymmetrical arrangement of atoms or molecules along different spatial directions, which causes the crystal to exhibit different refractive indices for different polarisation states. Engineered birefringence[24] arises from artificially introduced subwavelength anisotropic structures rather than from inherent properties of the material. This mechanism allows precise control over the birefringent behaviour by designing the geometry, orientation, and distribution of the structural elements at the nanoscale. Induced birefringence[25, 26] refers to the additional birefringence generated in a material by external influences such as stress, electric fields, magnetic fields, optical fields, and temperature changes.

Natural birefringence most commonly occurs in crystalline materials. In non-cubic crystals, the dielectric tensor becomes direction-dependent, endowing the crystal with an inherent birefringence. Crystals can be classified as uniaxial, having a single optical axis (e.g. calcite and quartz), or biaxial, having two optical axes (e.g. sodium nitrate and borax). Uniaxial crystals can be distinguished on the basis of their principal refractive indices. Positively uniaxial crystals satisfy $n_e > n_o$ (e.g., quartz), whereas negatively uniaxial crystals satisfy $n_e < n_o$ (e.g., calcite). Natural birefringence also occurs in certain polymeric materials. For example, uniaxially stretched polymer films exhibit inherent birefringence owing to their molecular orientation[27]. Additionally, some biological organic crystals, such as cellulose and collagen fibrils in corneal tissue[28], naturally exhibit birefringence. The differential interaction of polarised light provides the required contrast for biological polarisation imaging. It should be noted that natural birefringence varies with wavelength (material dispersion), yet is intrinsically a property of the material.

Engineered birefringence, also known as form birefringence, arises from the artificial structuring of isotropic materials into anisotropic sub-wavelength patterns. When the structural periodicity is significantly lower than the incident wavelength, the medium is regarded as an effective anisotropic material. This effective birefringence originates from the differences in the local dielectric constants and geometrical asymmetry, which induce distinct effective refractive indices for orthogonal polarisations. Under these conditions, the nanostructured region behaves as an effective medium, exhibiting optical anisotropy even though the constituent materials are isotropic. As schematically illustrated in Fig. 3(a), a typical unit structure consists of an asymmetric dielectric inclusion embedded in a substrate. By adjusting the geometric parameters such as length, width, height and orientation angle, one can precisely tune both the phase retardance and retardance axis orientation of the birefringence. Rather than being confined to simple rectangular geometries, anisotropic building blocks can adopt a wide variety of cross-sectional profiles, including elliptical[29], trapezoidal[30], and even freeform or irregular shapes[31] enabled by inverse and topology-optimisation design strategies. Meanwhile, the birefringent response can be further engineered through diverse structural configurations, such as multilayer or cascaded architectures[32], concentric and composite meta-atoms[33], as well as spatially graded arrangements with continuously varying geometrical parameters[34], thereby providing substantially expanded degrees of freedom for tailoring the effective birefringence. Thus, the engineered birefringence offers a powerful platform for realising compact, flat, and multifunctional photonic devices using subwavelength dielectric metastructures and metasurfaces with tailored polarisation properties.

Induced birefringence is a controllable effect that can be classified into the following types based on the induction mechanism. Stress-induced birefringence refers to the additional birefringence generated when a material experiences external mechanical or internal residual stress. The orientation of the retardance axis is directly linked to the principal stress direction in the material, and the magnitude of the phase retardance is quantitatively related to the stress through the photoelastic coefficient of the material. Stress-induced birefringence has two major engineering roles. It is widely used for the non-destructive inspection of internal stress in transparent media[35]. Optical glasses, lenses, polymers, and other transparent components often accumulate residual stress during fabrication and during cooling. Although these stresses are not visible through conventional visual inspection, they introduce slight direction-dependent changes in the refractive index. By measuring the birefringence, one can infer the magnitude, direction, and spatial distribution of internal stresses, thereby enabling quality control and process optimisation. Conversely, stress-induced birefringence can be precisely and actively controlled and applied[36]. In a photoelastic modulator (PEM)[37], mechanical or piezoelectric actuators impose high-frequency stress to dynamically tune the refractive index and rapidly modulate the polarisation (Fig. 3b). It is widely used for laser intensity modulation, beam stabilisation, and precision polarisation control.

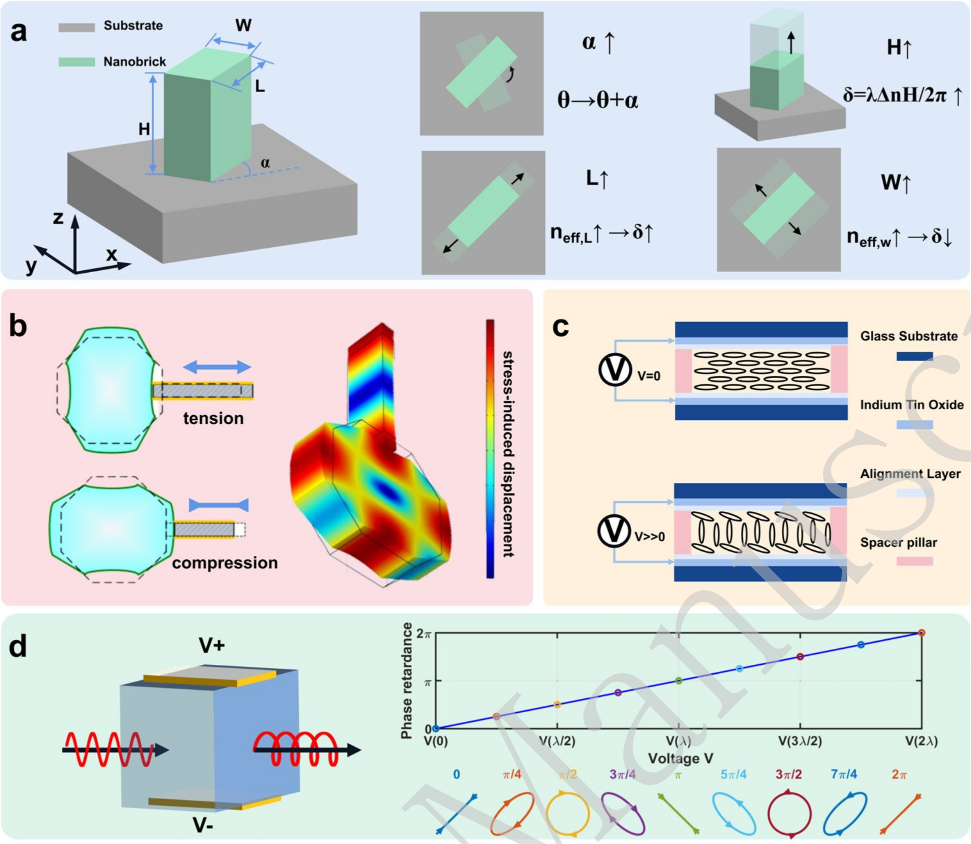

Fig. 3. Birefringence mechanism. (a) Engineered birefringence mechanism demonstrated by anisotropic metasurface nanobricks: the effective refractive indices along the long and short axes ($n_{eff,L}$ and $n_{eff,W}$) are independently controlled by the geometry of the nanobrick (length L, width W, height H) and in-plane rotation angle α, enabling tunable phase retardance δ and fast-axis orientation θ. (b) Stress-induced birefringence mechanism demonstrated via photoelastic modulator (PEM): stress induces optical anisotropy and displacement. (c) Electrically-induced birefringence mechanism demonstrated via liquid crystal variable retarder (LCVR): voltage alters liquid crystal alignment; (d) Electrically induced birefringence mechanism demonstrated via electro-optic modulator (EOM), enabling phase–voltage response and polarization control.

Electrically induced birefringence refers to the controlled differences in the refractive indexes under an applied electric field that causes birefringence. This effect enables dynamic phase delay modulation and is a core mechanism in optical control devices. Electrically induced birefringent materials include electro-optic (EO) crystals and liquid crystals (LC)[38]. EO crystals (e.g., $LiNbO_3$, KDP, BBO) use Pockels or Kerr effects to linearly or nonlinearly alter the refractive index tensor under an electric field, enabling precise polarisation and phase control (Fig. 3d). These devices respond in nanoseconds to picoseconds and are suitable for high-speed modulation[39]. The LC is a mesophase between ordered and disordered states[9, 40]. The rod-like molecules in nematic LC (Fig. 3c) exhibit optical anisotropy. Application of a field reorients the direction of the LC molecules, altering effective birefringence Δn_{eff} and enabling continuous phase retardance. Based on this principle, the LC variable retarder (LCVR) features low voltage, low power, and a simple structure. These two classes of devices are suitable for different modulation speeds and applications and form key implementations of electrically induced birefringence in modern photonics.

Additionally, magnetically-, thermally-, and photo-induced birefringences, although weaker or condition-dependent, are crucial for certain applications. Magnetically induced birefringence can produce a Faraday rotation (circular birefringence)[41]. When the magnetic field is aligned with the light path, it creates different refractive indices for the left- and right-circular polarisations, thereby rotating the plane of polarisation. Thermally induced birefringence refers to index changes due to thermal expansion or anisotropy under temperature gradients or heating[42]. In high-power optics, laser-generated heating in crystals creates temperature gradients, causing anisotropic index changes that distort the polarisation and wavefront, thereby affecting the stability and output quality. Photo-induced birefringence refers to the index anisotropy induced by molecular realignment, isomerisation, or photopolymerization under intense polarised light[43]. This is observed in photochromic materials and organic polymers, with birefringence persisting post-illumination, forming an "optical memory". Although weaker and slower, these effects uniquely enable thermal management, light-field control, and functional material studies, enriching induced birefringence mechanisms and applications.

Birefringence Types by Measurement Characteristics

Birefringence is typically characterised by two key parameters: phase retardance and retardance-axis orientation. Based on the temporal and spatial variations in these two parameters, common birefringent devices or samples can be categorised as static, dynamic, spatial, and spatiotemporal. Different types of birefringence impose varied technical requirements on the measurement methods used to assess their capabilities.

Static birefringence (Fig. 4a) refers to a fixed phase retardance and defined axis under constant conditions, yielding stable birefringence. Such birefringence is widespread in crystals, as exemplified by wave plates, which serve as core components for polarisation control and modulation[44, 45]. Static birefringence exhibits high repeatability and stability, which makes it suitable for high-precision and high-sensitivity measurements. Such measurements typically require only a single point or minimal sampling to accurately determine the phase retardance and retardance-axis orientation of the material for extracting the intrinsic birefringence coefficients, device quality control, and system modelling.

Dynamic birefringence (Fig. 4b) varies over time, generally with a fixed axis orientation, but with changing phase retardance. It can be divided into intentional modulation and unintentional drift. Intentional modulation refers to controlling birefringence via externally applied time-varying factors, such as EO modulators (EOM), LCVR, and PEM, thereby giving it an irreplaceable advantage with bandwidths ranging from kHz to GHz. Unintentional drift denotes birefringence fluctuations induced by environmental changes. For example, in fibre applications, the environmental temperature and stress vary diurnally or with loads/disturbances, causing slow drift or random changes in fibre birefringence[46]. Additionally, processes such as crystal growth, film deposition, and curing cause evolving stress fields or anisotropy accumulation that leads to time-varying birefringence[47, 48], increasing the demand for real-time monitoring. Dynamic birefringence reflects temporal changes in materials and requires a high temporal resolution in measurement systems. In practice, if the retardance axis remains stable during dynamic birefringence, the polarisation modulation component of the measurement system can be simplified to measure only the dynamic phase retardance, thereby enabling rapid and transient measurements.

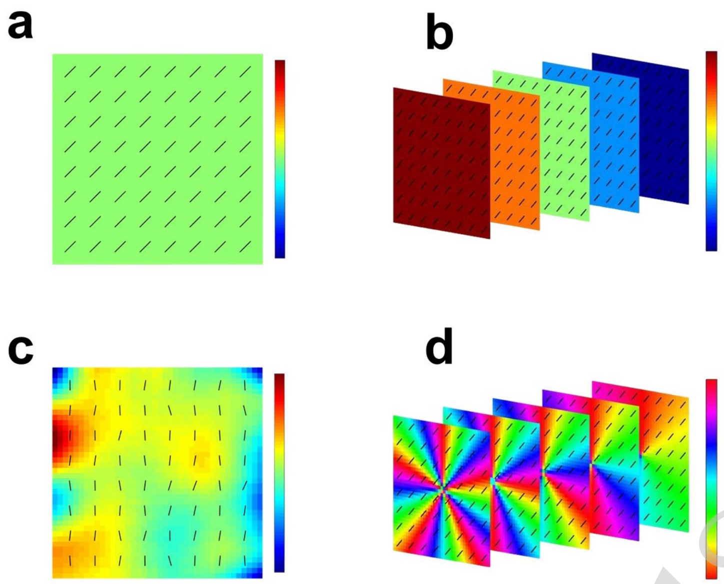

Fig. 4. Birefringence types by parameter characteristics: (a) static birefringence, (b) dynamic birefringence, (c) spatial birefringence and (d) spatiotemporal birefringence.

Spatial birefringence (Fig. 4c) refers to changes in the phase retardance and axis orientation at different locations, reflecting spatial anisotropy non-uniformity, which is widespread in various natural materials and engineered structures. For example, uneven stress or insufficient annealing can alter the index in different regions of optical components[49]. Fibres, muscles, and collagens in tissues also exhibit local birefringence owing to variations in orientation and density[50]. Additionally, vortex half-wave plates (VWP) and metasurface program axis orientation and retardance via spatially patterned anisotropy serve as spatially distributed devices[51]. Measuring the spatially distributed birefringence in applications requires a certain spatial resolution of the system. Typically, scanning systems acquire point-by-point 2D birefringence maps with high precision and flexibility, whereas wide-field imaging is well suited for large-area measurements. Notably, most spatial birefringence values show continuity or regional correlation, with the birefringent parameters varying gradually rather than randomly.

Spatiotemporal birefringence (Fig. 4d) integrates both temporal and spatial factors. Examples include an LC Spatial Light Modulator (LC-SLM)[52] and a tunable element[53] whose local birefringence updates rapidly under voltage or field drives, forming real-time tunable phase surfaces. In biomedicine, collagen regeneration and realignment cause local tissue birefringence to change continuously during burn healing, reflecting repair dynamic[54]. Analysing spatiotemporal birefringence requires capturing large field-of-view changes at a high time resolution, requiring systems with high-speed detection, real-time imaging, and multidimensional processing. Similarly, if the fast-axis orientation remains fixed, the measurement scheme can be significantly simplified, as in dynamic birefringence measurements.

Birefringence Measurement Method

Optical polarisation-based birefringence measurement is one of the most important methods for investigating the properties of anisotropic media, and fundamentally relies on detecting changes in the polarisation state of light as it propagates through a birefringent medium. From a technical perspective, birefringence measurement methods are generally categorised into three types: polarimetric modulation analysis methods, interferometric techniques, and other approaches. In recent years, continuous advancements in this field have led to significant improvements in the measurement accuracy and application scope. Regardless of the specific methods of implementation, all of these methods follow the same Jones-Mueller polarisation formalism and can be consistently described within the Jones or Mueller matrix framework.

Unified polarization framework for linear birefringence retrieval

The Jones and Mueller formalisms represent two widely adopted theoretical frameworks for describing the interaction between polarised light and optical media and constitute the fundamental theoretical basis for virtually all polarisation techniques. In fact, all birefringence measurement approaches introduced in the following sections are derived based on, or equivalently formulated within, the Jones or Mueller formalism.

In a generalised polarisation metrology framework, the optical response of a linearly birefringent sample, characterised by the phase retardance δ and the fast-axis orientation θ, can therefore be uniformly described using the following Jones matrix representation.

$$\begin{aligned} J(\delta,\theta) &= R_J(-\theta)J_S(\delta)R_J(\theta) \\ &= \begin{bmatrix} \cos\theta & \sin\theta \\ -\sin\theta & \cos\theta \end{bmatrix} \begin{bmatrix} 1 & 0 \\ 0 & e^{i\delta} \end{bmatrix} \begin{bmatrix} \cos\theta & -\sin\theta \\ \sin\theta & \cos\theta \end{bmatrix} \\ &= \begin{bmatrix} \cos^2\theta + \sin^2\theta e^{i\delta} & \cos\theta\sin\theta(1-e^{i\delta}) \\ \cos\theta\sin\theta(1-e^{i\delta}) & \sin^2\theta + \cos^2\theta e^{i\delta} \end{bmatrix} \end{aligned} \tag{1}$$

By applying rotational transformations to the canonical birefringence matrix, the linear birefringence operator at arbitrary orientations can be constructed from the observed Jones matrix, or similarly, from its corresponding Mueller matrix representation as follows:

$$\begin{aligned} M(\delta,\theta) &= R_M(-2\theta)M_S(\delta)R_M(2\theta) \\ &= \begin{bmatrix} 1 & 0 & 0 & 0 \\ 0 & \cos2\theta & -\sin2\theta & 0 \\ 0 & \sin2\theta & \cos2\theta & 0 \\ 0 & 0 & 0 & 1 \end{bmatrix} \begin{bmatrix} 1 & 0 & 0 & 0 \\ 0 & 1 & 0 & 0 \\ 0 & 0 & \cos\delta & \sin\delta \\ 0 & 0 & -\sin\delta & \cos\delta \end{bmatrix} \begin{bmatrix} 1 & 0 & 0 & 0 \\ 0 & \cos2\theta & \sin2\theta & 0 \\ 0 & -\sin2\theta & \cos2\theta & 0 \\ 0 & 0 & 0 & 1 \end{bmatrix} \\ &= \begin{bmatrix} 1 & 0 & 0 & 0 \\ 0 & \cos^2 2\theta + \sin^2 2\theta\cos\delta & \cos2\theta\sin2\theta(1-\cos\delta) & -\sin2\theta\sin\delta \\ 0 & \cos2\theta\sin2\theta(1-\cos\delta) & \sin^2 2\theta + \cos^2 2\theta\cos\delta & \cos2\theta\sin\delta \\ 0 & \sin2\theta\sin\delta & -\cos2\theta\sin\delta & \cos\delta \end{bmatrix} \end{aligned} \tag{2}$$

The Jones formalism is based on complex electric field amplitudes, and characterizes the transformation of polarisation states through a linear operator acting on the Jones vector. It provides a coherent field description and is therefore suitable for fully polarised and mutually coherent optical fields, allowing a direct and explicit representation of phase- and amplitude-related polarisation effects, such as linear and circular birefringence, as well as linear and circular dichroism, in non-depolarising optical systems. In contrast, the Mueller formalism is established in the intensity domain and describes the transformation of the Stokes vector through a real 4×4 matrix. It offers a statistical representation of the polarisation states and is applicable to partially polarised light and depolarising samples. Consequently, Mueller matrices can characterise not only deterministic polarisation transformations, but also depolarisation and polarisation mixing effects that cannot be captured within the Jones framework. However, the absolute optical phase is inherently discarded in the Stokes–Mueller representation, which constitutes a fundamental limitation for coherence-based measurements. In particular, birefringence is mapped solely through intensity-based quantities, and first-order phase effects arising from coherent superposition cannot be directly described within the Mueller formalism. Therefore, these two formalisms provide complementary yet unified descriptions of the same underlying polarisation response, forming the theoretical foundation of modern polarisation metrology.

For a given measurement configuration and system operation, the linear birefringence parameters of the samples are retrieved using the following general reconstruction model:

$$X = R(H,Y) \tag{3}$$

Here, $X \in \{J(\delta,\theta), M(\delta,\theta)\}$ denotes the polarisation response operator of the sample under the linear birefringence model and can be represented by either a Jones or Mueller matrix. Y denotes the experimentally acquired measurement data such as intensity sequences, interferograms, beat-frequency signals, spectral responses, multichannel pixel measurements, and related observables. H represents the known measurement configuration and system operation, including the light source, optical layout, modulation strategy, detection, signal-processing chain, and relevant instrumental settings. R denotes a reconstruction (or retrieval) operator that estimates the sample polarisation response X under the linear birefringence model from the measured data Y, given a known measurement configuration and system operation H. Eq. (3) constitutes a general inverse problem for estimating linear birefringence parameters.

Within this unified framework, existing linear birefringence measurement techniques reported in the literature can be categorised according to the level of polarisation information retrieved and the modelling assumptions adopted. Without loss of generality, they can be summarised into the following representative classes, ordered from more comprehensive to simplified system implementation:

(1) Full Jones or Mueller matrix measurements followed by parameter decomposition, in which the complete polarisation response is first reconstructed, and linear birefringence parameters are subsequently separated.

(2) Direct estimation of the linear-birefringence Jones or Mueller model, where the measurement model is explicitly constrained to a linear retarder and the parameters δ and θ are retrieved from the measured data based on the proposed model.

(3) Retrieval of phase retardance δ only under a linear birefringence model, where the fast-axis orientation θ is neglected or assumed to be fixed, and only δ is estimated.

(4) Qualitative or partial polarisation parameter extraction, in which only coupled or individual polarisation features derived from the Jones or Mueller representation are obtained to indicate birefringent behaviour.

Although these approaches differ in system complexity, data dimensionality, and computational cost, they share the same underlying matrix representation of the sample response and can be consistently formulated within the unified measurement and reconstruction framework introduced above. This unified modelling framework provides a common theoretical foundation for polarimetric modulation analysis, and interferometric and other techniques and highlights the intrinsic connections between the Jones- and Mueller-matrix-based implementations under the specific scope of linear birefringence characterisation.

Polarimetric modulation-analysis Technology

The polarimetric modulation-analysis method is based on measuring the intensity of polarised light and usually includes three modules: a polarisation state generator (PSG) in the light source, a sample under test, and a polarisation state analyser (PSA) in the detected light. First, the PSG unit adjusts the polarisation of the incident light via modulator elements to satisfy the measurement requirements. As light is transmitted through the birefringent sample, its polarisation state undergoes quantifiable changes. Finally, the PSA module detects the output polarisation changes to quantify the birefringence characteristics of the sample. The birefringence parameters of a sample can be accurately quantified based on various system models. Depending on the type of polarisation modulator used, typical methods include simple polarimeters and waveplate, EO, PE, and magneto-optic (MO) modulations.

The simple polarimeter is a classic instrument for analysing birefringence in transparent media and is the most widely used tool in the industry. It features an extremely simple structure and low cost. Only two polarisers are required to detect the hidden birefringence information that is undetectable using conventional methods. The core architecture of commercial birefringence measurement systems (e.g. Strainoptics PS-100, Laika Visoria-P[55], Nikon Eclipse Series[56], etc.) typically includes a broadband light source, a polariser, a sample, an analyser, and a CCD camera (Fig. 5a). Without the sample, the crossed polarisers yield a dark field on the CCD. During the measurement, the birefringence of the sample converts the linear polarisation into elliptical polarisation. After passing through the analyser, the interference colours on the CCD reveal the birefringence of the sample. Owing to the continuous spectrum of the broadband light source, the phase retardance map for different colours and chromaticity is qualitatively read from the pre-calibrated retardance-colour tables. This method is simple and intuitive but ignores the effect of the orientation of the retardance axis. The chromaticity errors are significant, allowing only qualitative assessments. Wang et al.[57, 58] proposed measuring both the phase delay and axis orientation simultaneously. Unlike traditional methods, a laser is used as the light source and the polariser axes are set to 60°. Rotating the waveplate yields the max/min intensities and angles for computing the parameters. The laser intensity fluctuation is monitored to eliminate source instability effects. Despite the compact and low-cost setup, it is difficult to operate and lacks precision. Minzioni et al.[59] analyzed the refractive index and birefringence of transparent media over a broad spectral range. Birefringent media like $LiNbO_3$ show different refractive indices over different spectral ranges. By analysing transmission changes in that range, birefringence can be measured across a wide band (0.7–1.65 μm) simultaneously. Cao et al.[60] used this setup to study the field-induced birefringence dynamics and derived the complex DC Kerr coefficients of chalcogenide glasses. With a fixed retardance axis, aligning the incident polarisation direction to a preset angle reveals the dynamic birefringence changes. Precise transmission and dynamic phase-retardance analyses yield the real and imaginary Kerr coefficients, revealing its nonlinear optical behaviour.

Driven by advances in precision manufacturing and emerging polarimetric devices, polarization cameras are gaining a central role; they simplify optical detection, and can be broadly categorized into division-of-time[61, 62], division-of-amplitude[63], division-of-aperture[64, 65], and division-of-focal-plane[66, 67] architectures, with recent developments further incorporating metasurface-based spatially multiplexed designs for compact and snapshot polarimetric imaging[68]. Lane et al.[69] implemented birefringence distribution measurements using a polarisation camera (Fig. 5b). The polarisation camera provides four polarisation analysis channels at 0°, 45°, 90°, and 135°, enabling simultaneous measurements of the corresponding linear polarisation components. Because it cannot cover all angles, the external polarisers are rotated multiple times to gather data for a set of Stokes parameters. The fitting algorithm matches these data to a theoretical model to determine the phase retardance, axis orientation, degree of polarisation, and other parameters. The polarisation camera based on the microlinear polariser array can simultaneously measure only the first three Stokes parameters (S0-S2), but not the circular component S3; therefore, it cannot directly acquire the complete parameters in a single snapshot. By introducing controllable polarisation modulators, this limitation can be effectively overcome by encoding the information of all the Stokes components, including S3, into the measured S0–S2 signals. For example, Wang et al.[70] demonstrated that by acquiring a set of input–output Stokes measurements, the complete Mueller matrix of the sample can be reconstructed using only six modulation states, implemented with a polarisation camera combined with dual rotating retarders. A more compact solution is provided by LC-based polarization cameras. Ye et al.[71] demonstrated an electrically regulated polarimetric camera based on a single twisted nematic LC chip in which electrically tunable LC elements were integrated directly in front of a CMOS sensor and rapidly switched by voltage control to realise solid-state polarisation modulation without any moving parts. An alternative solution for accessing the circular polarization component S3 is to employ planar nanostructured polarisation analysers that spatially multiplex multiple polarisation projections onto a single sensor, thereby enabling snapshot full-Stokes measurements without temporal modulation. Belle et al.[72] proposed a spatially resolved real-time polarimetric measurement method based on a hollow waveguide array. It uses a directional waveguide array with an analyser and CMOS camera to form the PSA. The hollow waveguide array introduces artificial birefringence by design, allowing direct measurement of the Stokes parameters (S0–S3) at a spatial resolution without moving parts. It achieves 50 µm² resolution and fast, real-time polarisation measurement. With no moving parts or single-shot measurements, the proposed system is compact and efficient for precise optical applications. Metasurface-based full-Stokes polarisation cameras have recently emerged as an important method for ultracompact and integrated polarization sensing[73, 74]. By engineering subwavelength anisotropic and chiral meta-atoms, metasurfaces can directly map different polarisation components to independent spatial, spectral, or intensity channels, enabling the single-shot acquisition of all four Stokes parameters without mechanical scanning or temporal modulation. Organic semiconductors[75, 76], metal-halide perovskites[77, 78], and two-dimensional materials[79, 80] can be directly employed as active materials for fabricating polarisation-sensitive photodetectors and cameras. The integration of metasurface polarisation control elements with these novel photodetector platforms offers a promising pathway toward compact, alignment-free, and highly integrated polarimetric imaging systems for quantitative linear birefringence measurements in on-chip and high-speed applications.

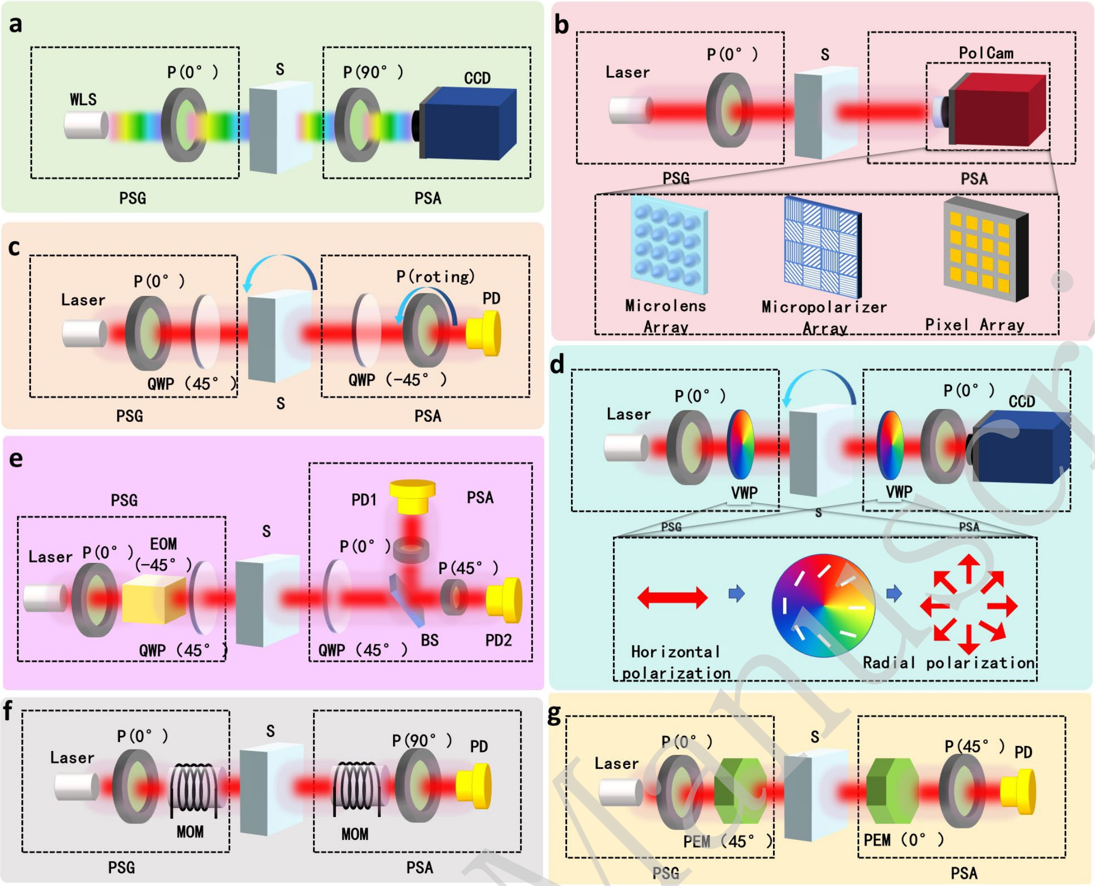

Fig. 5. Typical polarimetric modulation analysis technologies. Simple polarimeter with orthogonal polarizers[55] (a) and polarization camera[69] (b). Birefringence measurement system modulated by waveplate (c), VWP[81](d), EOM[82](e), MOM[83](f) and PEM[84](g). The abbreviations of the components in the systems above are as follows: Polarization State Generator (PSG); Polarization State Analyzer (PSA); sample (S); polarize (P); quarter-wave plate (QWP); vortex waveplate (VWP); electro-optic modulator (EOM); photoelastic modulator (PEM); magneto-optic modulator (MOM); beam splitter (BS); photodiode (PD); charge-coupled-device camera (CCD); polarization camera (PolCam); white-light source (WLS).

Waveplate modulation methods offer greater freedom of modulation, improved measurement accuracy, and applicability. A single wave plate or a combination of wave plates can more precisely control light polarisation and directly measure sample birefringence via intensity changes under different polarisation states. Waveplate modulation methods employ various implementations and measurement principles. The Tardy quantitative method (Fig. 5c) uses a laser to reduce the dispersion effects and requires the retardance axis of the sample to be parallel to the polariser axis. The sample must be rotated around the surface normal, and the analyser is turned to minimum intensity. The phase retardance is then calculated from the precise quantitative relationship between the retardance-axis orientation of the sample and the analyser's rotation angle. Although this method accounts for the orientation of the retardance axis and improves the accuracy, it is cumbersome and unsuitable for rapid measurements. Wu et al.[85] proposed a high-speed spatiotemporal birefringence measurement method. Unlike Tardy, the first QWP rotates at high speed, and the CCD is a 10 kHz camera, which captures the axis orientation and retardance changes under load. Its core feature is a sequential analysis method that uses multiple-intensity images to rapidly build a spatiotemporal birefringence map, which delivers high-precision real-time data under dynamic loads and serves as an effective tool for tissue and failure analysis. Pretka et al.[86] analysed the sensitivity of small dynamic retardance measurements. The PSG of the system comprises a polariser and Wollaston compensator, whereas the PSA consists of a QWP, polariser, and CCD. By matching the dynamic retardance-axis orientation to a system-dependent reference orientation and precisely adjusting the azimuth of each optical element, the system maximises the fringe-phase contrast, allowing the precise measurement of phase-delay changes by analysing fringe shifts. The experiments show 6000× sensitivity gain and 0.003° accuracy. Despite the sensitivity boost, it attains a peak sensitivity over a very limited range and is extremely cumbersome, limiting its practical use. Moreover, studies indicate that polarisation optic demodulation for birefringence measurement is generally nonlinear, causing the sensitivity to vary nonlinearly across the measurement range. Lin et al.[87] used a Zeeman laser to generate dual-frequency orthogonal beams, and proposed a novel birefringence method. Under an applied magnetic field, the atomic energy levels in the laser medium split according to the Zeeman laser principle. The system comprises a Zeeman laser, HWP, QWP, sample, QWP, polariser, and PD. It measures birefringence distributions in PEN films etc. by scanning, with standard deviations of axis orientation and phase retardance errors of ≤0.20° and ≤0.52°, respectively. Zeeman lasers are less stable than single-frequency lasers. Field stability directly affects the laser output frequency and measurement results. In environments with large field fluctuations, the measurement stability may suffer. In addition to conventional uniform waveplates, novel spatial light polarisation control plates, such as DOE waveplates, have recently attracted wide interest. They provide more control freedom, uniquely modulating the beam polarisation, and offering an efficient measurement tool for more complex optics. The most representative is the zero-order VWP, an optical element combining standard half-wave behaviour with vortex-beam characteristics. VWP (Fig. 5d) achieves a 180° phase delay and, by introducing a helical phase, maintains a constant phase retardance across the aperture, while its fast axis continuously rotates, thus generating radial polarisation. Chen et al.[88] proposed a new measurement method using the VWP. After passing through the test plate, the polarisation state of the beam changes, affecting its intensity distribution. In this method, the test plate is rotated to capture two distinct intensity-change patterns. Rotation alters the relative orientation to ensure full interaction between different polarisation states. The results show measurement errors of approximately 0.087° for the phase retardance and 0.094° for the fast axis angle, demonstrating high precision and feasibility. Zhu et al.[81] improved upon this using radial polarisation and analysers in both stages (Fig. 5e), and achieved single-shot measurements with no mechanics involved. Unlike traditional methods, they introduced a Fourier analysis instead of conventional mean intensity calculations to effectively avoid source fluctuation effects. This method not only achieves stable phase retardance measurements (standard deviation $< 0.3°$) but also high-precision fast-axis angle measurements (average absolute error $< 0.04°$).

Another strategy for achieving high-precision and efficient birefringence measurements is to introduce dynamic birefringent-device modulation. Dynamic modulation not only provides real-time monitoring of a sample's birefringent characteristics but also effectively enhances the measurement sensitivity and accuracy. The aforementioned birefringence measurement methods often rely on static polarisers or waveplates, adjusting the light polarisation by rotating the waveplate or polariser. These have limitations such as system complexity, cumbersome operation, and a strong dependence on rotation angles. Dynamic birefringent device modulation introduces tunable optical elements such as EO, MO, and PEM modulators, enabling real-time polarisation control without the physical rotation of components, thereby precisely controlling the beam's polarisation and phase without moving the optical systems. These methods render birefringence measurements more flexible, faster, and adaptable to various experimental requirements. Lo et al.[82] (Fig. 5e) used an EOM with sinusoidal modulation and processed signals via Fourier–Bessel expansion, simultaneously measuring the retardance-axis orientation and phase retardance in linear birefringent materials. System errors mainly originate from the misalignment of the electro-optic modulator and defects in the optical components, especially the misalignment of the EOM, which causes significant errors. However, the system showed good repeatability, with an average error of 0.186° for the axis angle and 0.356° for the phase retardance. Li et al.[83] (Fig. 5f) proposed a high-precision glass internal stress measurement method using the MOM. By combining two independent MOMs to adjust the polarisation states, the birefringence induced by glass stress is obtained, and the system maintains high stability under environmental changes, offers strong adaptability, and effectively enhances the signal amplitude while reducing noise interference. The experiments showed a precision of 0.3 nm/cm. However, owing to the small Verdet constant of magneto-optic materials, even under strong magnetic fields, the Faraday rotation angle produced is limited, resulting in an insufficient polarisation modulation amplitude. The analyser-converted intensity after modulation varies quadratically with the rotation angle, rendering the fundamental component extremely small. This makes signal demodulation difficult, results in high dispersion, and because a small amplitude requires long integration and averaging to improve the signal-to-noise ratio (SNR), leading to lengthy measurements that limit practicality. The PEM method[84, 89] is a mainstream commercial solution for high-precision birefringence measurements. Using high-frequency polarisation modulation of the PEM, the detected signal carries both the PEM modulation frequency and birefringence information of the sample (Fig. 5g).

Using the DC, fundamental and second harmonic components, phase retardance, and axis orientation are simultaneously solved, achieving rapid online calibration measurement of phase retardance and fast-axis orientation in the same path, with a single-point measurement time of 20 ms, phase delay resolution < 0.043 nm, and relative error < 0.71%.

In a broad range of situations, the polarisation response of a sample may involve not only linear birefringence but also dichroism, circular anisotropy, and depolarisation. Mueller matrix measurements based on a polarimetric modulation-analysis framework have recently attracted increasing attention for achieving complete characterisation of the polarisation properties. This is achieved at the expense of increased system complexity compared with methods specifically designed for linear birefringence measurement. Linear birefringence measurement can be regarded as a particular case within the Mueller matrix measurement. The conventional Mueller matrix measurement system[90] employs wave plates and linear polarisers such as PSG and PSA to generate and analyse a more diverse and complex set of polarisation states than approaches limited to linear birefringence. In principle, at least 16 intensity images corresponding to independent PSG–PSA state combinations are required to reconstruct the complete 4 × 4 Mueller matrix. This approach provides complete and quantitative polarimetric information. However, it relies on multi-frame sequential acquisition and mechanically rotated components, which lead to limited temporal resolution and increased sensitivity to sample motion and system drift. Yu et al.[91] employed a more sophisticated PSG capable of simultaneously generating a pair of complementary incident polarisation states within a single configuration, including 0°/90° and 45°/135° linear polarizations, and right-/left-circular polarisations. Using these three complementary pairs of incident polarisation states, the complete Mueller matrix can be reconstructed from only three acquisitions, significantly improving the measurement efficiency. Feng et al.[92] reported an ultrafast method in which multiple polarisation projection states were spectrally encoded using a specially designed PSG–PSA architecture and subsequently converted into a single time-domain waveform through an optical time stretch, from which the Mueller matrix was reconstructed using a calibrated linear inversion model. This architecture enables single-shot, nanosecond-scale Mueller matrix measurements for dynamic processes; however, it assumes a wavelength-invariant Mueller matrix and relies on a complex single-point ultrafast system, limiting its applicability. Oh et al.[93] realized an ultra-wide-field spectroscopic Mueller matrix imaging system in which both the polarisation state generator and analyser were implemented using dual rotating wire-grid polarisers, enabling pixel-wise reconstruction of the Mueller matrix spectra over a field of view of approximately 20 mm × 20 mm. This strategy delivers high-throughput, spatially resolved polarimetric and spectroscopic information, but relies exclusively on linear polarization modulation, restricting the measurement to a reduced 3 × 3 Mueller matrix, and the required multi-state and multi-wavelength acquisition further limits its suitability for dynamic measurements. With the rapid development of nanofabrication and lithography technologies for polarisation optics, Zaidi et al.[94] proposed a compact single-shot system based on spatially multiplexed metasurfaces in which both PSA and PSG were implemented using metasurface optics that encode multiple polarisation projection channels into the different spatial regions of a single image, enabling complete Mueller matrix reconstruction from a single camera exposure. By shifting the polarisation modulation from the temporal to the spatial domain, this work establishes a fundamentally new instrumentation paradigm and demonstrates how metasurfaces introduce additional design freedom for polarisation systems, opening new opportunities for polarisation detection and sensing.

Table 1 compares the performance of the different modulators used in the aforementioned methods, which helps to quickly identify the strengths and weaknesses of each device in terms of mechanism, bandwidth, and modulation depth, and thus choose the solution that best meets the experimental requirements. Other polarimetric modulation analysis techniques[95-97] exist that focus on innovations or improvements in polarisation modulation, polarisation analysis, and signal demodulation.

Table 1. Comparison of Polarization Modulation Devices

Device	Modulation Type	Actuation Mechanism	Modulation Frequency	Modulation Range	Typical Materials
Fixed Waveplate	Static Birefringence	Static	-	Any Birefringence	Quartz, MgF_2, polymer, mica
Rotating HWP	Dynamic retardance axis	Mechanical Rotation	<100 Hz	Axis orientation 0–180° with time	
VWP	Spatial retardance axis distribution	Static	-	Axis orientation 0–90°with spatial azimuth	fused silica, Liquid-crystal polymer
EOM/ LCVR	Dynamic phase retardance	Electric field	kHz – GHz /DC-1kHz	Typical retardance range 0–π rad	$LiNbO_3$, KTP, BBO/ Nematic liquid crystal
PEM	Dynamic phase retardance	Piezo-driven stress	~20–100 kHz	Typical retardance range -π/2–π/2 rad	Fused silica, BK7
MOM	Dynamic optical rotation	Magnetic field	< 1kHz	Typical rotation range (< π/4)	TGG, YIG

Interferometric Technology

Interferometric methods rely on the principle of optical interference to calculate birefringence by measuring the phase difference, intensity variations, and other characteristic features of the interference signal. Interferometer designs mainly include traditional interferometer configurations and novel self-mixing interferometer structures. Traditional interferometer configurations include but are not limited to Michelson, Mach–Zehnder, Sagnac, and Fizeau interferometers. Based on the Michelson interferometer, Del Hoyo et al.[98, 99] (Fig. 6a) split an incident beam into two orthogonal linear polarisations using a polariser. The mirror of one arm is slightly tilted to produce high-contrast interference fringes, the test waveplate is then inserted before recombination, and after passing through a 45° analyser, the fringes are recorded by a camera. As the wave plate rotates, the fringes shift laterally. The fringe displacements and rotation angles were repeatedly recorded throughout the full rotation of the wave plate, and the data were fitted to calculate the birefringence parameters. Polarisation-sensitive OCT (PS-OCT)[100, 101] is a low-coherence Michelson interferometer that uses a superluminescent diode (SLD) or swept-source (SS) laser as the light source. The beam is split into reference and sample arms, and the reflected or backscattered light is interferometrically detected (Fig. 6b). PS-OCT is widely used for quantitative birefringence measurements in semitransparent scattering samples (e.g. biological tissues and filled polymers)[102, 103]. Unlike in conventional OCT, the returned light is first passed through a polarisation beam splitter into two orthogonal polarisation channels (commonly labelled S and P), which are then synchronously detected using a dual-channel detector to acquire low-coherence interference signals. The local phase retardance and orientation of the retardance axis were calculated by comparing the phases of the two channels at the same depth. However, because PS-OCT relies on detecting backscattered light, fully transparent, non-scattering materials produce no usable backscatter signals, rendering it incapable of internal tomography in such media. Therefore, transmission-mode optical methods are required to measure the birefringence in fully transparent media.

Compared to the Michelson interferometer configuration, the Mach–Zehnder interferometer spatially separates the reference and sample arms completely, facilitating the insertion of polarisation control elements or modulators into the sample arm without disturbing the polarisation state of the reference arm. Moreover, because the paths of the two arms are independent, an acousto-optic modulator (AOM) or EOM can be placed in each arm to achieve heterodyne interference or phase modulation, thereby enabling high-sensitivity lock-in detection and improving the measurement accuracy and dynamic range of the phase retardance. Lang et al.[104] used a Mach–Zehnder interferometer based on heterodyne interference (Fig. 6c), in which two AOMs generated an approximately 60.32 kHz beat-frequency carrier while recording horizontal and vertical polarisation interference signals. They then used maximum likelihood estimation to extract the signal amplitude and phase and independently solved them in real time to determine the phase retardance and axis orientation of the

LCVR, requiring no mechanical adjustment to suppress environmental disturbances and common-mode noise, thus providing key performance metrics for high-speed, wide-range birefringence characterisation. Wei et al.[105] employed a fibre-based Mach–Zehnder interferometer combined with MEMS micromirror scanning, which achieved large-aperture, non-contact, and full-surface stress measurements. A 1550 nm distributed feedback laser source was passed through an AOM to generate an 80 MHz frequency-shifted beam that interfered with the test beam. The polarisation beam splitter recorded the intermediate-frequency signals of the horizontal and vertical components, which were demodulated using a digital signal processing system using the phase difference between the two heterodyne signals. Thus, the optical path delay of the sample was directly obtained, allowing the stress value of the sample to be calculated. The system's phase detection accuracy reached 5×10^{-5} rad. For a 2 mm-thick fused quartz sample, the stress measurement accuracy reached 1.8 kPa with a relative error of less than 0.01%, meeting the requirements for high-speed, wide-range, high-precision stress characterisation.

Certain specialised interferometer configurations demonstrate advantages in various application scenarios. Schnoor et al.[106] implemented dynamic birefringent element measurements based on a Sagnac interferometer (Fig. 6d). Using a common-path interferometer built with a pair of polarisation beam splitters and symmetrical mirrors, the LCVR sample produced a phase difference between two counter-propagating beams. The phase retardance was inverted from the lateral displacement of the interference fringes recorded by the camera. Compared with traditional crossed or co-polarizer methods, this approach effectively suppresses intensity of noise while directly applying FFT for fringe phase calculation and unwrapping to achieve real-time mapping between the phase retardance δ of the LCVR and the drive voltage V, thereby characterising the key performance metrics of a high-speed, wide-range birefringence measurement system. Furthermore, the Sagnac interferometer has a ring common-path structure that inherently cancels environmental disturbances, vibrations, and thermal drifts. This scheme ensures high sensitivity and a wide dynamic range, while avoiding the complex path matching and mechanical adjustments required in the Michelson and Mach–Zehnder beam-splitting designs. It requires only one coupler and a segment of a polarisation-maintaining fibre for full fibre integration, thus giving it an irreplaceable advantage in fibre stress birefringence measurement[107, 108]. Tan et al.[109] introduced a polarisation-adjustable phase-shift principle with a rotatable polariser using a Fizeau interferometer (Fig. 6e). The Jones matrix model describes how phase-shift interferometry can be achieved by inserting a linear polariser in a common optical path and rotating it to 0°, 45°, 90°, and 135°. The residual birefringent phase retardance and the orientation of the retardance-axis at each pixel can be directly determined by combining and differentiating the four phase-shift results without the noncommon-path matching required by the Mach–Zehnder design. In testing large-aperture optical elements having a 230 mm diameter aperture, this method achieved a peak-valley (PV) repeatability of 0.1 nm/cm (standard deviation 0.029 nm/cm), and a spatial resolution at sub-millimeter scale. Compared to traditional commercial polarimeters, the test time was reduced from over half an hour to a few minutes, greatly enhancing the rapid, high-precision detection of residual birefringence in large-aperture optical materials.

Traditional interferometry demands reference–measurement interactions, yielding high complexity. As a special configuration, self-mixing interferometry (SMI)[110, 111] treats the intracavity field of the laser as the reference beam, eliminating the need for an external reference arm and effectively reducing system complexity. Moreover, self-mixing exhibits a richer phenomenon than traditional interferometry. The feedback interaction with the intracavity field leads to a new dynamic balance in the amplitude, phase, frequency, and polarisation of the laser. Additionally, self-mixing integrates the source and detector, and the intracavity field serves as a reference and amplifies the interaction with feedback with a gain of up to 10^6, leading to a simple optical path, easy collimation, and high sensitivity[112]. Polarisation effects in SMI involve three key phenomena: orthogonal component phase difference[113], polarisation flipping[114], and amplitude–phase modulation[115, 116]. The first two effects apply to quasi-isotropic lasers, whereas the latter applies to anisotropic lasers. Quasi-isotropic lasers, such as Nd:YAG, He–Ne, and VCSELs, have isotropic gain media, but the complex output polarisation is affected by intracavity stress, external forces, pump power, and pump polarization[117, 118]. The addition of feedback introduces complex dynamics. The residual random stress induces a slight anisotropy in the refractive index of the laser crystal, causing frequency splitting into two orthogonal polarisation modes. Mode competition favours the polarisation closest to the gain peak, resulting in a well-defined polarisation state. Consequently, at low pump levels, quasi-isotropic lasers emit single-mode linear polarisation in arbitrary orientations. However, feedback can readily shift the competition balance and alter the output polarisation. The orthogonal component phase-difference method[119] (Fig. 6f) uses a polarisation beam splitter with its decomposition axes at 45° to the initial polarisation of the laser; the two orthogonal outputs are detected separately. With the birefringent sample in the external cavity, the laser output shifts from linear to a slightly elliptical polarisation, generating a fringe phase difference. With the PZT-driven mirror motion, the phase difference peaks when the retardance axes align. The birefringence was calculated as the ratio of the maximum phase difference to the sample retardance and alignment angle. This method is simple and accurate, but requires sample rotation, making it complex and unsuitable for spatially varying birefringence. The polarisation flipping method[120] (Fig. 6g) adopted at higher feedback levels than the phase difference method. When the retarder axis is parallel or perpendicular to the initial polarisation of the laser, the sample induces a flipping point in the fringes. The output shifts from a single linear mode to alternating dual-orthogonal modes. This is because the effective reflectivities of both the polarisation modes are modulated. The mode with higher reflectivity experiences lower cavity losses and thus preferentially reaches the lasing threshold. The flipping region peaks when the sample retardance axis aligns with the initial polarisation. The birefringence was obtained from the duty cycle of the flipping region. This method is simple and accurate; however, its measurement procedure is complex.

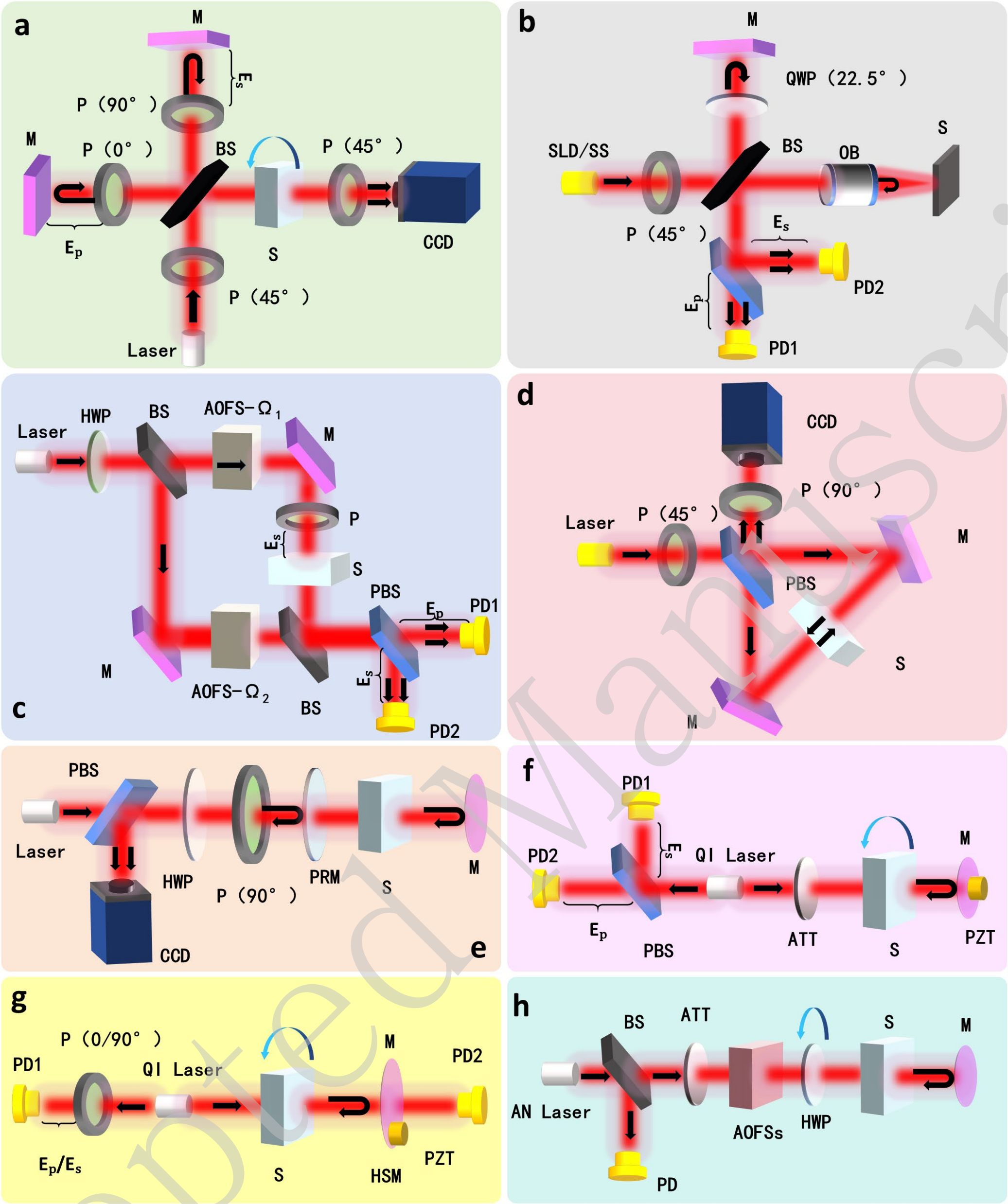

Fig. 6. Typical interferometric technologies. Birefringence measurement system based on Michelson interferometry[98](a-b), Mach-Zehnder interferometry[104] (c), Sagnac interferometry[106](d), Fizeau interferometry[109] (e) and Self-Mixing interferometry (f-h). (b) OCT[100], essentially a reflection-mode low-coherence Michelson interferometer. Self-Mixing interference by the method of orthogonal phase difference[119](f), polarization flipping[120] (g) and amplitude-phase modulation[121] (h). The abbreviations of the components in the systems above are as follows: mirror (M); polarizing beam splitter (PBS); half-wave plate (HWP); objective (OB); superluminescent diode/swept-source laser (SLD/SS); acousto-optic frequency shifter (AOFS); shifted frequency (Ω); attenuator (ATT); piezoelectric transducer (PZT); quasi-isotropic (QI); anisotropic (AN); partially reflecting mirror (PRM); p- and s-polarized component (Ep/Es).

Later studies found that these two effects also depend on both external birefringence and intracavity stress[122]. Intracavity stress is difficult to control precisely, meaning that lasers with varying internal stresses exhibit different feedback behaviours, reducing measurement accuracy and increasing unpredictability and instability. In contrast, anisotropic lasers have inherently anisotropic gain media, exhibiting significant differences in output characteristics and feedback effects compared with quasi-isotropic lasers. For example, in Nd:YVO_4 lasers, the gain spectrum is polarisation-dependent: the π-polarised emission (parallel to the crystal axis) is much stronger than the σ-polarised. The large difference in gain ensures that the π mode always prevails, yielding stable π-polarised output conducive to the controlled measurements. With optical feedback, the Nd:YVO_4 laser maintains a linear polarisation output, avoiding the polarisation instabilities observed in quasi-isotropic lasers and enabling stable and controllable operation. A birefringence measurement method based on Nd:YVO_4 feedback polarization[121] (Fig. 6h) uses frequency-shift modulation to move the detection signal to 2 MHz, avoiding low-frequency noise. Polarisation modulation using a rotating half-wave plate replaces the sample rotation, reduces complexity, and enables multifunctional measurements of static, dynamic, and spatial birefringence. Results show standard deviations of 0.0453° in phase retardance and 0.0939° in axis orientation, with sample transmittance down to $\sim 10^{-5}$.

These interferometric methods reviewed above mainly aim to quantify linear birefringence parameters such as phase retardance and retardance-axis orientation, and are therefore well-suited for characterising the principal anisotropy of transparent media. Similarly, to achieve a complete characterisation of the coherent polarisation transfer properties, holographic interferometric approaches[123] also enable full Jones matrix measurements, in which linear birefringence is naturally included as a particular case. In general, the full Jones matrix can be obtained by the object wave interfering with polarisation-orthogonal reference waves and reconstructing the complex vectorial optical field from a multiplexed hologram, from which the complete complex Jones matrix is directly retrieved by relating the recovered orthogonal field components to the known incident polarisation states. Li et al.[124] proposed a single-shot, dual-wavelength, and polarisation-multiplexed scheme based on Kramers–Kronig (KK) holographic multiplexing, in a modified Mach–Zehnder interferometer, in which partial spectral overlap enabled significantly improved spatial bandwidth utilisation while ensuring the retrieval of the full complex Jones matrix. Owing to its noniterative reconstruction and single-shot acquisition, real-time Jones matrix imaging at video rate (30 fps) is demonstrated, making this technique particularly attractive for the dynamic birefringent samples. Qiu et al.[125] introduced a single-shot off-axis polarisation holographic Jones matrix measurement method assisted by KK relations, where the polarisation-resolved holograms are simultaneously recorded by a polarisation camera, and analytic-signal reconstruction is used to remove the autocorrelation terms, leading to a markedly enlarged usable spatial bandwidth and an approximately 2.12× improvement in resolution while maintaining real-time capability. Liu et al.[126] proposed a single-shot common-path polarisation holographic scheme with partially coherent illumination, in which two mutually orthogonal polarisation states simultaneously illuminate the sample, and polarisation- and angle-multiplexed holograms are generated and recorded in a common-path configuration to reconstruct the full complex Jones matrix. The system exhibits improved phase stability and effective suppression of speckle and parasitic interference; however, its reliance on Fourier-plane spatial filtering and dual-camera acquisition increases the system complexity and calibration demands. Liu et al.[127] presented a compact single-shot Jones matrix imaging system based on polarisation in-line holographic microscopy, in which two orthogonal illumination states (±45°) are generated simultaneously and a polarisation beam displacer maps the four polarisation-resolved in-line holograms onto different regions of a single CCD, forming a fully common-path and highly compact optical layout without a separate reference arm, enabling complex-field reconstruction and subsequent synthesis of the full Jones matrix within one exposure. These single-shot Jones matrix measurements enabled the observation of transient anisotropy and rapidly evolving polarisation dynamics. In practice, the achievable temporal resolution is primarily limited by the camera frame rate and exposure time, together with the computational cost of complex-field reconstruction and matrix retrieval, particularly when iterative holographic phase retrieval or twin image suppression is required.

To provide a systematic overview of the differences in the structural complexity and measurement capabilities of the different interferometric configurations, Table 2 summarises five representative designs—Michelson, Mach–Zehnder, Sagnac, Fizeau and Self-Mixing—highlighting their reference/measurement arm arrangements, support for transmission and reflection modes, heterodyne or lock-in detection capabilities, and other key characteristics. This comparative summary allows researchers to quickly grasp the strengths and limitations of each architecture and select the most appropriate interferometer for a given application.

Table 2. Comparison of Interferometric Structures for Birefringence Measurement

Interferometric Structure	Structural Complexity	Characteristics
Michelson	Medium	Separated reference/measurement arm; transmission-mode measurement (except OCT in reflection mode).
Mach-Zehnder	High	Separated reference/measurement arm; transmission-mode measurement; heterodyne configuration Support.
Sagnac	Relatively High	Loop configuration with counter-propagating beams; bidirectional transmission-mode Measurement; excellent noise immunity.
Fizeau	Relatively Low	Partially common-path reference/measurement arms; transmission/ reflection -mode measurement
Self-Mixing	Low	No separate reference arm (intracavity reference); transmission-mode measurement; heterodyne configuration Support.

Other Polarization optical Technology

In addition to polarisation modulation analysis and interferometry, a distinctly different class of polarisation optical birefringence measurement techniques exists. One example is a method that exploits the system’s own physical effects for birefringence measurement, such as the frequency-splitting method[128, 129]. In this method, a birefringent element (e.g. wave plate or sample) is placed inside a linearly polarised laser cavity. A small birefringence causes a slight difference in the refractive indices between the horizontal and vertical eigenmodes, leading to the splitting of their resonance frequencies. By capturing the beat signal of the two modes using a high-speed photodetector and an RF spectrum analyser, one can measure the frequency difference Δf precisely. Then, using $\Delta\varphi=2\pi\Delta f\cdot L/c$ (where L is the effective intracavity path length and c is the speed of light), the phase retardance Δφ is computed to quantify birefringence. This method has a simple setup and is inherently robust against vibrations and temperature drift. Its measurement range spans 0–π, resolution reaches the 10^{-3} rad level, and experimental uncertainty is below 0.0036 rad.

Another representative approach uses computational imaging algorithms to probe birefringence[130, 131]. For example, Zhang et al.[132] proposed a birefringence measurement method that combines PIE, which enhances precision by introducing a diffractive element. In this method, a rotating polariser changes the polarisation state and diffraction patterns are recorded at different polariser angles. Diffraction is analysed using PIE to reconstruct the phase and amplitude. The advantage of this method is its ability to provide high-precision quantitative results for complex materials, particularly those that traditional methods struggle to handle, such as opaque or structurally intricate samples. Park et al.[133] proposed a synthetic-aperture-based Jones matrix synthesis algorithm in which multiple Jones matrices acquired under different illumination angles are coherently combined in the complex domain to substantially suppress the coherent phase noise and enhance the polarisation sensitivity of weakly birefringent samples. This approach enables high-sensitivity Jones matrix imaging of living eukaryotic cells, benefiting from the strong noise suppression and physically transparent, non-iterative processing based on direct field synthesis and eigen-analysis, at the expense of reduced temporal resolution and increased stability requirements because of the need for multi-angle and multi-frame acquisitions. Dai et al.[134] introduced a vectorial Fourier ptychography algorithm to reconstruct complex-valued Jones matrices over a large field of view and beyond the diffraction limit, with the additional capability of jointly correcting polarisation-dependent system aberrations. While this method enables complete and physically consistent Jones matrix reconstruction with high spatial resolution, its iterative Gauss–Newton optimisation and joint system–sample estimation lead to a relatively high computational cost.

Applications

Transparent and translucent materials play vital roles in everyday life, modern industrial manufacturing, aerospace technology, and contemporary scientific research. This section systematically examines the demand for birefringence measurements across four domains: stress analysis, materials science, biomedical applications, and the characterisation of novel polarisation-optical components.

Residual stress analysis

Internal stresses from post-processing annealing or external forces during installation often induce anisotropic stress and orientation, altering the local density and converting an originally isotropic medium into an anisotropic one, thereby causing stress birefringence[135, 136]. Polarisation optical methods serve as classic tools for analysing the stress distribution and orientation by visualising stress via birefringence. Typically, the birefringent optical path difference per unit thickness is used to express stress magnitude, satisfying $\delta = \Delta\varphi \cdot \lambda / t$, where $\Delta\varphi$ is the phase retardance, λ is the probe laser wavelength and t is the material thickness. The magnitude of the phase retardance is proportional to the principal stress, and the retardance axis indicates the direction of the principal stress.

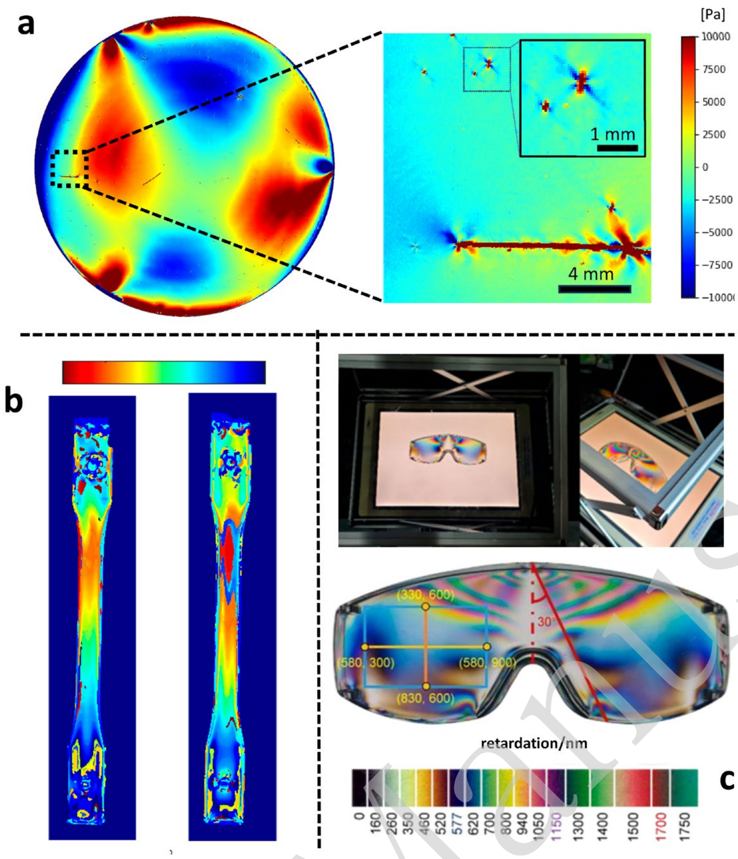

Fig. 7. Residual stress analysis. (a) Shear stress distribution of silicon wafer[137], where the colour map represents the spatial distribution of the in-plane shear stress and the inset highlights the localized stress concentrations. Reproduced under CC BY-NC-ND 4.0. Copyright 2024, Elsevier. (b) Distribution of residual stresses in the injected part[138], corresponding to two processing conditions. Reproduced under CC BY 4.0. Copyright 2023, MDPI. (c) Photoelastic images of the polycarbonate goggle[139], showing the experimental setup, the stress distribution and the corresponding colour bar from top to bottom. Reproduced under CC BY-NC-ND 4.0. Copyright 2023, Frontiers Media.

Kovács et al.[137] (Fig. 7a) performed in-situ shear stress imaging on 300 mm single-crystal silicon wafers. The fixture load sites exhibited clear stress concentration, reflecting a direct load response. Meanwhile, the maps revealed significant stress anomalies at the internal defects under loading. The stress maps clearly reveal edge stress gradients and identify minute defects, providing direct evidence for wafer defect screening, edge quality assessment, defect traceability, and coordinated optimisation with processes such as ion implantation and annealing, thereby contributing to yield improvement and shortening production adjustment cycles. Vargas-Isaza et al.[138] (Fig. 7b) conducted a study on thermoplastic injection-moulded parts and systematically evaluated the distribution of residual stresses under different moulding conditions and their effects on mechanical performance. The residual stress in these parts was predominantly flow-induced, with peaks ranging from 4.29 to 5.69 MPa—well below the flexural failure stress. Raising the mould temperature (80 °C) and packing pressure increased the part density and flexural strength but also elevated the residual stress, whereas the longer packing times slightly reduced it. These results offer quantitative guidance for the quality control, process optimisation, and service life assessment of high-precision transparent optical components. Wang et al.[139] (Fig. 7c) focused on a rapid qualitative evaluation method for the residual stress in injection-moulded polycarbonate goggles. By extracting the average gray values from specific regions of the goggle lenses or along selected sampling lines and combining experimental testing with analytical evaluation, a correlation was established between the residual stress distribution and warpage deformation. Through the optimisation of process parameters—including mould temperature, melt temperature, injection speed, packing time, and cooling time—the maximum residual stress in the lenses was reduced by 59.7% to 4.874 MPa, and warpage deformation was reduced by 74.2% to 0.18 mm, significantly improving the moulding quality and dimensional stability of the product. This provides an efficient and practical approach to defect control and process optimisation of transparent polymer optical components. Moreover, birefringence stress measurements hold significant value for stress evaluation and control in glass products (particularly transparent structural components for aerospace)[140, 141], semiconductor products (such as photovoltaic modules[142] and thin films[143]), and precision optical elements[144]. In stress testing, birefringence measurements are key for assessing the internal stress, orientation, and anisotropic defects. On the one hand, it supports research, development, and failure analysis, for example, mapping stress to identify structural weak points; on the other hand, it has entered production lines for quality control, such as online inspection of plastic optics and monitoring high-performance composite manufacturing. As the demand for precision fabrication increases, birefringence analysis plays a larger role in stress evaluation.

Material characterization

Birefringence measurement is also a key method for revealing the optical anisotropy and structural tuning behaviour of crystalline materials[145, 146]. It has not only become an important approach for assessing material structural integrity but also provides critical characterisation support for understanding structural evolution under various growth conditions, heat treatment states, and external field modulation, playing a significant role in high-quality crystal fabrication and material design optimisation.

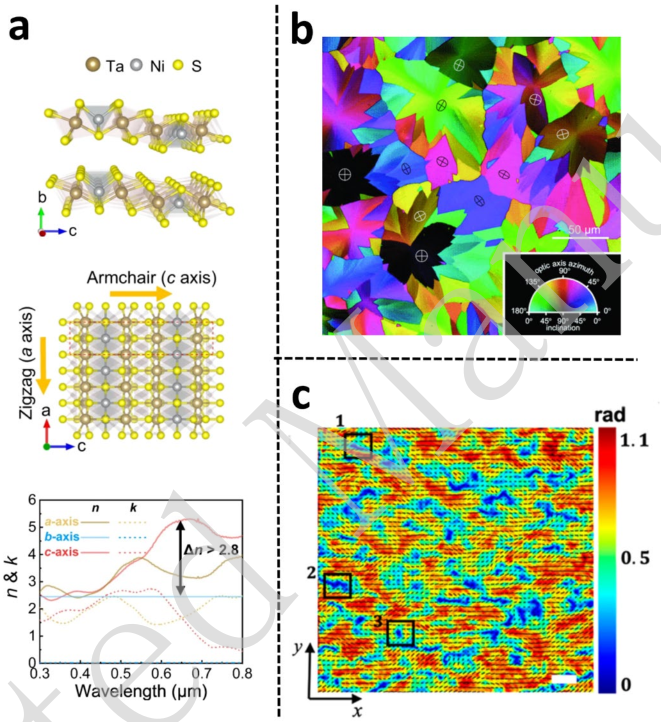

Fig. 8. Material characterization. (a) Structure and refractive-index values of Ta$_2$NiS$_5$ crystal[147], showing the principal refractive indices along different crystallographic axes and the pronounced in-plane optical anisotropy. Reproduced under CC BY 4.0. Copyright 2023, Springer Nature. (b)Image of a thin polycrystalline calcite film of uniform thickness[148], where the colour contrast reveals the spatial distribution of the crystal orientations and local optical anisotropy among individual grains. Reproduced with permission. Copyright 2008, John Wiley & Sons. (c) Retardance and orientation angle maps for a flowing liquid crystal[149], showing the spatial distributions of birefringence. Reproduced with permission. Copyright 2021, American Chemical Society.

Recently, 2D van der Waals materials have attracted attention owing to their layered structure and strong anisotropy, resulting in ultrahigh birefringence. Multiple studies have shown that these materials achieve refractive index differences far exceeding those of traditional crystals from the visible to infrared bands[147, 150]. For example, As$_2$S$_3$ exhibits Δn ≈ 0.4 in the visible range[151], and Ta$_2$NiS$_5$[147] shows Δn ≈ 2.8 in the mid-infrared range (Fig. 8a), surpassing classical optical materials such as calcite and rutile. Extreme in-layer covalent/ionic versus interlayer van der Waals bonding causes high refractive index contrasts, yielding strong optical anisotropy. Additionally, some 2D materials feature non-centrosymmetric or bilayer modulations, boosting nonlinear birefringence[152]. In the above studies, birefringence measurements were required to retrieve the complex refractive index, enabling quantitative mapping of wavelength-dependent birefringence, while also serving as an important means to reveal the complex birefringence behaviour in anisotropic crystals. Oldenbourg [148] imaged a uniform-thickness polycrystalline calcite film (Fig. 8b), encoding the optical axis azimuth in hue and the inclination angle in brightness, thereby obtaining a quantitative birefringence map over the entire field of view. Within individual crystalline domains, the hue and brightness were highly consistent, indicating uniform birefringence properties, whereas abrupt changes at the grain boundaries reflected discontinuities in the c-axis orientation. Bouhy et al.[153] reconstructed the retardance and optical-axis orientation distribution of a composite geological thin section from sparse measurement data, thereby significantly reducing the measurement time while preserving the grain-level spatial resolution. Cao et al.[154] used birefringence measurements to sort micron-sized crystals precisely. At the wavelength of 546.1 nm, they systematically examined birefringence of Al_2O_3, SiO_2, KDP, LBO, and BBO samples with different sizes. Birefringence measurement is not only valuable for studying heterogeneous and topologically complex crystalline materials but also constitutes a critical analytical technique for investigating emerging materials. Ge et al.[149] investigated the birefringence of lyotropic liquid crystals in microfluidic channels, acquiring the retardance and orientation angle distributions in real time at speeds up to 506 fps (Fig. 8c), thereby revealing structural formation and evolution during flow. By tracking the low-retardance regions, this technique quantitatively captures the local structural changes and dynamic features under steady-state flow, providing direct and precise experimental evidence for understanding the flow behaviour and orientational response of lyotropic liquid crystals. Overall, birefringence measurements play an important role in the quantitative characterisation and validation of research into novel materials. The analysis of the polarisation responses assesses the achieved anisotropy and guides structural and performance optimisation. With the emergence of new anisotropic materials, birefringence parameters have become key metrics for evaluating the performance of photonic functional materials and for geological mineral analysis.

Biological detection

Biological tissues, either sectioned or within the superficial layer (typically 5–50 μm), exhibit good optical transparency, allowing light to penetrate and carry rich structural and molecular information. This localised transparency provides favourable conditions for birefringence measurement, making it an essential foundational tool for biological imaging, pathological diagnosis, and histological analysis.

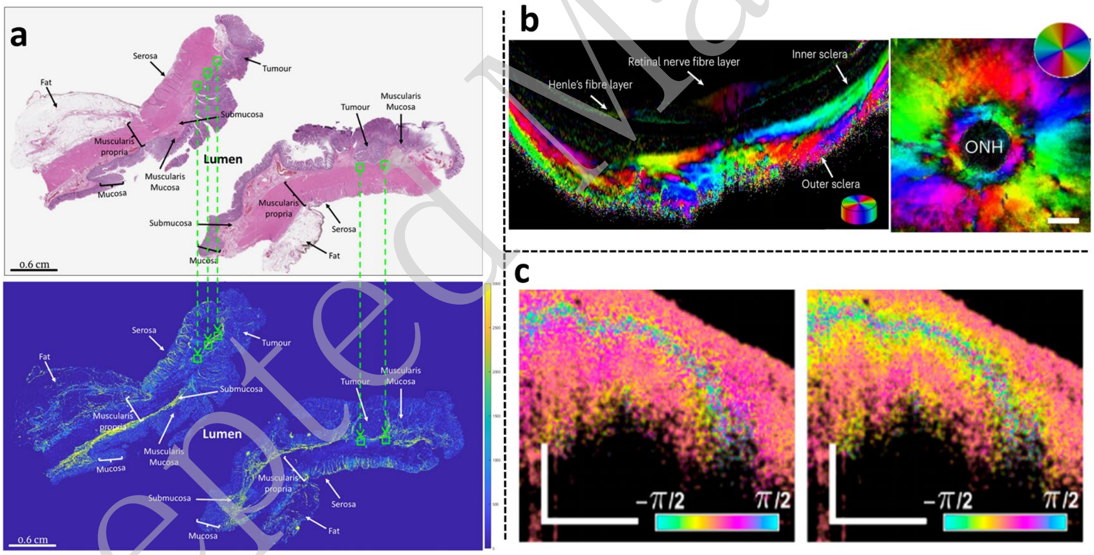

Fig. 9. Biological detection. (a) Comparison between H&E-stained histology image (top) and corresponding polarimetric intensity image (bottom)[155]. Reproduced under CC BY 4.0. Copyright 2022, Springer Nature. (b) The posterior sclera images by OCT[156], including a depth-resolved image (left) and an en-face image (right). Reproduced under CC BY 4.0. Copyright 2023, Springer Nature. (c) Linear retardance maps of basal cell carcinoma along different polarization directions[100]. Reproduced under CC BY 4.0. Copyright 2017, MDPI.

Recently, birefringence measurements have shown unique advantages in tumour detection and pathology. Owing to its polarisation sensitivity, birefringence imaging reveals microstructural and anisotropic information that is inaccessible using conventional microscopy[155] (Fig. 9a). Retardance axis orientation maps reveal changes in orientation within tissues, reflecting the ordered structure and remodelling the characteristics of collagen fibres, cell arrangements, and other features. Liu[156] used quantitative imaging to study the birefringence distribution of the posterior sclera (Fig. 9b) and found that the posterior scleral birefringence (PSB) is closely related to the orientation and diameter of collagen fibres, which reflects changes in the tissue microstructure. PSB showed an increasing trend around the optic disc and posterior pole with higher degrees of myopia and could distinguish between patients with high myopia and those with pathological myopia, outperforming traditional indicators such as axial length. This study indicates that PSB can serve as a structural biomarker for early identification, monitoring, and prediction of myopia progression, providing new quantitative evidence for the timing of clinical intervention. Phase-retardance images provide quantitative information on the anisotropy strength and can sensitively capture optical anisotropy enhancements caused by variations in tissue density, fibre content, and abnormal growth. Different tumour types are significantly different from normal tissues in terms of their microstructure and optical anisotropy, leading to distinct changes in their birefringence properties. Birefringence measurement not only enables contrast-based differentiation between the normal and diseased regions but also assists in pathological grading and boundary determination. This approach has been successfully applied for the detection of various tumours, including skin cancer[100] (Fig. 9c), breast cancer[157], colorectal cancer[158], and brain tumors[159]. In digital pathology and intraoperative diagnosis, birefringence images offer a non–haematoxylin and eosin (H&E) information dimension, complementing multimodal analysis. Moreover, Mueller matrix imaging[160] can be used to obtain complete full-polarisation parameters (such as depolarisation, diattenuation, and birefringence characteristics), further enabling the multidimensional quantitative characterisation of the optical properties of tissues. In biomedical imaging, birefringence measurement provides label-free, intrinsic contrast without staining and is capable of revealing tissue microstructure and pathological changes. It is a powerful tool for early cancer screening and diagnosis, intraoperative guidance, and tissue engineering evaluation.

Calibration of novel optical devices

Novel polarisation optical elements (e.g. LCVR, VWP, and birefringent metasurfaces) play a key role in precision optics and advanced photonic devices, and their performance directly determines a system’s polarisation-control capability and imaging/measurement accuracy. These elements often exhibit strong spatial anisotropies and complex structures, which increase the calibration requirements for accurate birefringence characterisation.

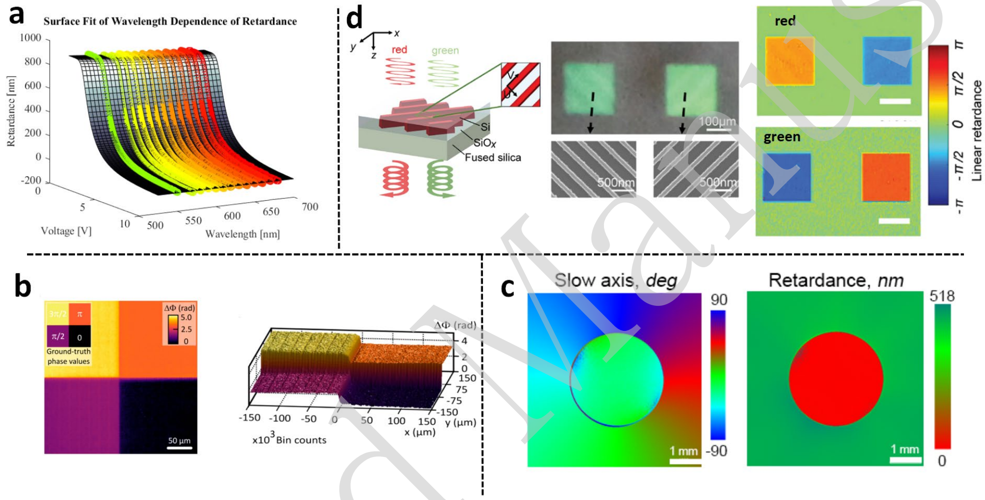

Fig. 10 Calibration of novel optical devices. (a) Phase retardance of the LCVR at different wavelengths[106]. Reproduced under CC BY 4.0. Copyright 2020, Optical Society of America. (b)Three-dimensional phase visualization of LC-SLM[161], showing the loaded phase pattern on the LC-SLM (left) and the reconstructed phase distribution (right). Reproduced with permission. Copyright 2021, American Chemical Society. (c) Birefringence measurements of manufactured hollow S-waveplate [162], showing the spatial distributions of the slow-axis orientation (left) and the phase retardance (right). Reproduced under CC BY-NC-ND 4.0. Copyright 2022, Elsevier. (d) Si metasurface image [163]. From left to right, the panels show schematic illustration of the metasurface structure and functionality, optical microscope image (top) and SEM image (bottom), and linear retardance images under red (top) and green (bottom) illumination. Reproduced under CC BY 4.0. Copyright 2024, Wiley-VCH.

The LCVR features a wide dynamic range of birefringence, enabling rapid phase-retardance changes via the drive voltage (Fig. 10a). Although LCVRs offer large apertures, high control precision, and stable optical and chemical performances, the relationship between phase retardance and drive voltage is nonlinear and can exceed 2π, requiring precise calibration of the voltage–birefringence dynamic response before use[106]. The liquid crystal spatial light modulator (LC-SLM)[161] is essentially a programmable array of LCVR which is capable of precisely encoding optical wavefronts and enabling dynamically tunable two-dimensional spatial birefringence distributions. It is widely used in high-precision optical systems such as wavefront control, holographic imaging, and polarisation modulation[164]. However, variations in the phase uniformity, nonlinear response, and thermal drift among different pixels under varying driving conditions can lead to degraded system performance or functional deviation if not accurately measured and calibrated. Therefore, quantitative phase retardance measurement of the SLM under actual operating conditions not only helps to determine its true dynamic phase modulation capability but also provides essential data for compensating pixel-to-pixel differences, optimising driving strategies, and improving wavefront control accuracy (Fig. 10b). Vortex retarders (VWP)[162], made from birefringent liquid crystal polymers, generate higher-order beams such as vector polarisation and vortex beams. Structurally, an ideal VR provides a constant π/2 phase retardance across its aperture with a continuously rotating fast-axis orientation over the optical region; thus, uniformity of retardance and continuity of axis orientation reflect the quality of VWP fabrication (Fig. 10c). In recent years, metasurfaces have become a research focus in modern optics owing to their subwavelength-scale control of the phase, amplitude, and polarisation. Among these, anisotropic metasurfaces are the primary technological routes for realizing metasurface waveplates[165]. Compared to conventional crystalline waveplates, they are thinner, offer greater functionality, and enable programmable control. Numerous metasurface-based wave plates for wavelength, angle, and polarisation multiplexing, as well as optically and electrically triggered dynamic plates, have been reported[51, 166]. The modulation performance of a birefringent metasurface fundamentally depends on the spatial accuracy of the phase retardance δ and axis orientation θ, as well as their spectral and angular dispersions (with wavelength and incidence angle). These devices comprise arrays of subwavelength anisotropic elements that impart different complex transmission/reflection coefficients to the polarisation components (Fig. 10d), thereby enabling pixel-level light-field control and achieving high-efficiency polarisation conversion, wavefront shaping, and holographic imaging. The corresponding birefringence detection requires multiple wavelengths, directional flexibility, and high-speed measurement. δ(x,y) and θ(x,y) should be quantitatively and traceably characterised under the target numerical aperture and field-of-view conditions, thereby closing the design–fabrication–verification–optimisation loop. Using birefringence measurements, spatially resolved imaging of the phase retardance distribution and axis orientation of these optical elements can be achieved, enabling a comprehensive evaluation of their polarisation-control performance, which is crucial for design optimisation and quality control.

COMPARISON OF DIFFERENT TECHNIQUES

Table 3. Comparison of birefringence measurement methods. δ, phase retardance; θ, retardance axis; std, standard deviation; MAE, mean absolute error; RMS, root mean square error; MinAE, minimum absolute error; RE, relative error; R^2, Coefficient of Determination.

Method	Accuracy		Technical characteristics	Limitations	Applicable Range	Ref
	δ	θ				
Simple polarimeter (Colour Observation)	~200nm	-	Low cost, simple system, and intuitive observation	Neglect of retardance axis, only qualitative measurement, and need for rotating the sample to achieve better viewing	Suitable for low-precision spatial and large birefringence, e.g., stress analysis, material/biological observation	55, 56
Simple polarimeter (Laser-Based)	std 0.48° @632.8 nm	std 0.32°	Low cost, simple system, and suppression of laser fluctuation by dual-path	Need for sample rotation to modulate signal, complex operation, high requirement for detector polarization response, and limited functionality of complex/spatial imaging.	Suitable for static and dynamic birefringence, e.g., calibration of arbitrary waveplate and EOM	57, 60
Simple polarimeter (Polarization Camera)	std 0.005 rad @ 526 nm	std 0.1°	Simple system, and support for large-area spatial birefringence mapping	Need for polarizer rotation to enhance fitting accuracy, and systematic errors from pixelated polarizer arrays	Suitable for static and spatial birefringence, e.g., residual stress analysis, material /biological detection	69

Waveplate modulation (QWP rotation-Based)	Uncertainty 1°–2° @~546.1 nm	Uncertainty 5°–9°	Fully automated measurement, high-speed rotating QWP modulation, and high-speed measurement	Low measurement precision, random error induced by mechanical modulation, and requirement for stringent rotation mechanism and synchronization precision	Suitable for spatiotemporal birefringence, e.g., dynamic-response and microstructural-evolution monitoring of material /biological samples	85
Waveplate modulation (QWP-Based)	std ±0.05° @ 632 nm	std ±0.03°	High measurement precision, and polarization analyser utilization as detector	High cost, limited functionality, and QWP-precision–induced systematic error	Suitable for high-precision static birefringence e.g., calibration of arbitrary waveplate	167
Waveplate modulation (VWP-Based)	std < 0.3° @633 nm	MAE < 0.04°	No mechanical motion, frequency-domain demodulation, and one-shot measurement	Limited functionality, measurement accuracy limited by detector pixel size and systematic error caused by VWP machining precision	Suitable for high-precision static birefringence e.g., calibration of arbitrary waveplate	81
MO modulation	std 3.1 nm/cm @808 nm	std 2.3′	No mechanical motion, dual MO modulation structure, fully automated measurement, and lock-in amplifier–based demodulation	Low measurement efficiency; low fundamental-frequency signal due to weak MO effect, and signal detection and processing difficulty	Suitable for static birefringence and spatial birefringence with small area, e.g., residual stress analysis, material detection	83
EO modulation	detection limit (stress)	- (fixed θ)	No mechanical motion, reflection-type ellipsometer architecture, and high-speed	High cost, limited functionality, need for high-voltage drive, cumbersome measurement process, and systematic	Suitable for static birefringence and dynamic birefringence with high-speed, e.g., real-time stress	168

	7.84 kPa @633 nm		modulation and measurement (high up to GHz)	error caused by EOM dynamic modulation	analysis, and induced birefringence transient monitoring	
PE modulation	std 0.02 nm @632.8 nm	std 0.01°	No mechanical motion, high measurement accuracy, cascaded dual PEM configuration, and FPGA-based real-time signal processing	Need for initial system offset calibration to correct residual birefringence of the PEM, and speed limitation of spatial measurement by scanning imaging	Suitable for static, dynamic and spatial birefringence, e.g., residual stress analysis, material characterization, calibration of novel optical devices	84, 89
Michelson	std 0.88° @637 nm	RMS: ~1°	No additional waveplates or modulators (Uses only linear polarizers), suitable for multiple wavelengths, and fitting algorithm based	Complex structure, limited functionality, systematic error in fringe displacement, and fitting model sensitive to fringe distortion	Suitable for static birefringence e.g., calibration of arbitrary waveplate	98
PS-OCT	sensitivity ~0.01–0.1 rad	error: ~1°	Based on spectral-domain or swept-source, reflection configuration interferometry, and real-time depth-resolved measurement	Complex structure, error from speckle noise and multiple scattering, and inability to measure non-scattering homogeneous media	Suitable for spatial birefringence of back-scattering medium e.g., biomedical tissues imaging, and material anisotropic analysis	100

Mach-Zehnder	Uncertainty $\lambda/10^4$	Uncertainty < 1°	No mechanical rotation, heterodyne configuration interferometer, and real-time amplitude and phase extraction	Complex structure, requires matching of QWP retardance to reduce error	Suitable for high-precision static and dynamic birefringence, e.g., calibration of arbitrary waveplate, LCVR and EOM	104, 169
Sagnac	std ~2.1 nm	-	Common-path Sagnac interferometer, interference fringe phase tracking, and compatible with multiple wavelengths	Complex structure, requires alignment and image processing, zero-phase point needs a 45° rotation reference	suitable for high-precision polarization control and birefringence calibration, especially in fiber-optic systems	106, 107
Fizeau	std 0.029 nm/cm	-	Common-path configuration, four-step phase shift modulation, tunable and large test aperture, and compatible with tunable wavelength	Sensitive to polarizer rotation angle error, and return errors from polarizer surface flatness may introduce system errors	Suitable for high-precision spatial birefringence in large-aperture, e.g., residual stress analysis, material characterization, calibration of novel optical devices	109
Self-Mixing (Orthogonal phase difference)	std <0.1° @632.8 nm	- (fixed θ)	Simple system, frequency-domain demodulation, and anti-disturbance ability	Limited functionality, alignment error by Wollaston prism, inability to automatically measure retardance axis, and accuracy affected by intracavity anisotropy	Suitable for high-precision static birefringence e.g., calibration of arbitrary waveplate	119

Self-Mixing (Polarization flipping)	std 0.05° @632.8 nm	- (fixed θ)	Simple system, extracts birefringence via switching between distinct polarization states, and high-contrast modulation	Limited functionality, inability to automatically measure retardance axis, and lock-in phenomenon at weak phase retardance	Suitable for high-precision static birefringence e.g., calibration of arbitrary waveplate	170
Self-Mixing (Amplitude -phase modulation)	std 0.0453° @1064 nm	std. dev. 0.0939°	Compact configuration, high detection sensitivity, high repeatability accuracy, multifunction, heterodyne configuration	Systematic error due to half-wave plate precision limits, presence of mechanical rotation, and speed limitation of spatial measurement by scanning imaging	Suitable for static, dynamic and spatial birefringence with low transmittance, e.g., residual stress analysis, material characterization, calibration of novel optical devices	121
Frequency splitting	MinAE 0.0036 rad	- (fixed θ)	Simple system, high repeatability accuracy, high traceability, and applicable to weak birefringent phase retardance elements	Limited functionality, error from the internal components, and need for stable laser mode	Suitable for high-precision static birefringence e.g., calibration of arbitrary waveplate	129
Computational Optics	RE ~5.66%	R^2 ~0.986	No mechanical rotation or translation, lens-less configuration, iteration-based computation, and relatively wide field of view.	High cost, low measurement efficiency, low measurement precision, and requires computationally intensive iterative reconstruction	Suitable for static, dynamic and spatial birefringence, e.g., residual stress analysis, material characterization, calibration of novel optical devices	171

CONCLUSION AND PERSPECTIVES

Linear birefringence is widely present in crystals, polymers, glass, and tissues, and serves as a key measure of optical anisotropy. Polarisation optical measurement techniques have become important tools for birefringence analysis owing to their noncontact nature, high sensitivity, and multidimensional information acquisition capabilities. Current research has progressed from physical modelling and system design to algorithmic reconstruction and the development of a series of representative technical approaches that provide reliable tools for material stress detection, optical component characterisation, and biological tissue imaging. Although current birefringence measurement techniques have achieved diverse and significant advancements, key issues require focused attention for practical applications and further development.

Smaller system errors and stricter calibration: Birefringence measurement systems often include multiple birefringent optical components, and phase retardance errors or axis orientation deviations introduced during static or dynamic modulation can become critical factors affecting system accuracy[172, 173]. In particular, when measuring samples with extremely weak birefringence[174], such system errors may be comparable to or even exceed the birefringence of the sample, severely disrupting the measurement results. Therefore, more compact optical systems with fewer components are needed to minimize cumulative errors from multiple birefringent elements[171]; however, stricter and more physically based calibration methods are urgently required. Because polarisation effects in birefringent devices are combined using Jones or Mueller matrix multiplication rather than linear addition, calibration must start from a system matrix model that considers the polarisation behaviour of each component to establish an accurate error model and correction scheme[175, 176]. Additionally, for transparent samples, multiple reflections and interferences at the input and output interfaces can introduce extra phase errors. In high-precision measurements, index-matching fluids can reduce face-reflection effects, thereby improving the overall system stability and reliability of measurement.

High repeatability and random errors: In high-precision birefringence measurements, repeatability and system stability are key indicators of technical reliability. As research on multifunctional transparent materials has deepened, measurement techniques are evolving toward higher sensitivity and weaker signal detection[177], especially for subtle anisotropic changes induced by electric fields, magnetic fields, mechanical strains, and chemical environments, imposing stricter stability requirements. Measurement consistency depends heavily on the stability of key system components, including the power and wavelength stability of the light source and phase response stability of the modulation devices[178]. Improving the performance of these core components significantly enhances overall system repeatability. However, in intensity-based measurement methods, the system is susceptible to low-frequency environmental noise that causes fluctuations in the measurements. Techniques such as heterodyne interferometry, which shift signals to high-frequency regions, effectively avoid low-frequency noise interference[179], significantly improving the signal-to-noise ratio and system stability. Such frequency-shifting and demodulation strategies, combined with high-precision data acquisition and processing algorithms, offer a feasible path for achieving high repeatability and robustness in birefringence measurements.

Higher-dimensional information and decoupling of coupled multimodal information: As studies on material microstructures and optical behaviours continue to deepen in complex material systems such as anisotropic gradient structures, biological tissues, and multilayer films, characterisation of the comprehensive optical response requires not only multiple polarisation-related effects, but also sufficient spatiotemporal resolution and spectral information[180, 181]. Full-polarisation measurement techniques[182] based on Mueller matrix imaging provide an established solution for accessing the polarisation dimension and can simultaneously retrieve linear/circular birefringence, diattenuation, and depolarisation parameters, thereby enabling a comprehensive description of complex polarisation responses. Extending polarisation measurements in the time domain is particularly important for capturing dynamic polarisation variations in living biological tissues, such as microstructural remodelling, stress evolution, and physiological activities, and is also highly relevant to emerging studies on ultrafast laser–matter interactions[183, 184], where transient anisotropy and polarisation responses evolve on extremely short timescales. In this context, real-time and high-speed polarisation metrology[185, 186], particularly single-shot Jones matrix measurements[187], are of special significance because they enable direct access to coherent polarisation transfer properties and rapidly varying anisotropy while simultaneously providing the high temporal resolution and quantitative polarisation information required for dynamic biomedical and ultrafast applications. In parallel, the incorporation of spectral information enables the characterisation of dispersion-related birefringence and wavelength-dependent polarisation effects, which are critical for complex materials and nanostructured devices[188, 189]. To address the nonlinear coupling among multiple polarisation effects across spatial, temporal, and spectral dimensions[190], multi-angle, multi-wavelength, and polarisation-state modulation strategies, together with advanced inversion and reconstruction algorithms, are typically required to achieve reliable quantitative decoupling and physically interpretable polarization parameters[191, 192]. Multimodal and multidimensional information can provide a comprehensive description of the sample and is of great significance for quantitatively revealing the microstructural evolution in materials, the structural and functional states of biological tissues, and the underlying polarisation and light–matter interaction mechanisms in functional optical materials.

More intelligent functionality and convergence with emerging materials/ technologies: The rapidly growing diversity of demands on birefringence measurement is driving the development of measurement systems for higher functional integration, automation, and intelligence. Currently, birefringence measurement is no longer limited to single-mode measurements for uniform, stable elements (e.g. wave plates) but is gradually expanding to complex scenarios such as spatial distribution mapping, dynamic birefringence monitoring, and retardance axis (e.g. stress direction) extraction. Simultaneously, to meet the measurement demands for specialised materials and scenarios, such as low-transparency materials, nonspherical irregular structures, weakly birefringent samples, and high-speed dynamic changes[193], measurement systems must have greater adaptability and higher sensitivity. In addition, the practical implementation of birefringence metrology can involve complicated experimental procedures, tedious manual operations, and system debugging, which may limit the overall efficiency of measurement. Therefore, there is an urgent need to develop highly integrated systems with automatic axis alignment, autocalibration, intelligent recognition, and adaptive measurement capabilities to improve measurement convenience and stability[194]. In this context, machine learning, particularly deep-learning-based frameworks[195], is expected to play an increasingly important role in both front-end system design[196, 197] and back-end data interpretation[198, 199] for birefringence measurements, enabling breakthroughs in measurement efficiency, complex functionality, and adaptive control, thereby significantly enhancing system intelligence and application capabilities. Deep-learning-based data analysis provides powerful tools for rapid inversion, denoising, and quantitative decoupling of multiple coupled polarisation parameters[200, 201] and further enables advanced interpretation of measurement data, in which additional physical or structural information of the sample can be inferred from the birefringence-related measurements under appropriate models and priors[202, 203], thereby supporting automated and high-throughput analysis in complex measurement configurations. Emerging photonic materials and devices have reshaped the instrumentation paradigm of birefringence metrology. For example, polarisation cameras[204] enable snapshots and simplified polarisation detection, significantly reducing the system complexity and facilitating real-time operation. In parallel, metasurfaces and anisotropic metamaterials offer unprecedented flexibility for polarisation manipulation and multiplexed encoding[205], opening new routes for compact and application-specific birefringence sensing architectures[206]. The synergistic integration of advanced photonic devices with artificial-intelligence-assisted control and analysis is expected to substantially improve the measurement efficiency, functionality, and reliability, and to provide powerful technical support for future applications.

Although birefringence measurement is a classical field, it remains full of vitality and challenges due to the wave of new technologies. Future birefringence measurements will develop toward high precision, multifunctionality, and intelligence, thus becoming indispensable tools for understanding and optimising anisotropic materials and devices. As an important branch of optical measurements, birefringence measurements will continue to provide critical support for scientific research and engineering practice in the future.

Acknowledgements

This research was supported by the National Natural Science Foundation of China (Grant Nos. 62405292 and 62405135), Fundamental Research Program of Shanxi Province (Grant No. 202403021222184), Postdoctoral Fellowship Program of CPSF (GZC20240802 and GZC20242242), and Jiangsu Funding Program for Excellent Postdoctoral Talent (2024ZB744).

Author Contributions

S.W.: Writing—original draft, methodology, visualisation, and formal analysis. X.C. and K.J.: Writing—review, editing, and data curation. K. L., X. X., and Y.W.: Validation and formal analysis. J.W.: Investigation and editing. H.S. and Y.T.: Conceptualization, supervision, and funding acquisition.

Data availability

All data are available from the corresponding authors upon reasonable request.

Conflict of interest

The authors declare that there are no competing interests.

References

[1] Han, S.J. et al. Recent Development of SnII, SbIII-based Birefringent Material: Crystal Chemistry and Investigation of Birefringence. *Angewandte Chemie-International Edition* **62**, e202302025 (2023).

[2] De Lorenci, V.A. & De Paula, L.T. Light propagation in magnetoelectric materials: The role of optical coefficients in refractive index modulation. *Physical Review A* **112**, 013514 (2025).

[3] Steglich, P. & Kehrein, A. Light propagation in anisotropic materials and electro-optical effects: tutorial on the use of eigenvalue problems, tensors, and symmetries. *Journal of the Optical Society of America B-Optical Physics* **41**, 2191-2210 (2024).

[4] Cserti, J., Holló, A. & Oroszlány, L. Snell's law in multirefringent systems. *Physical Review B* **111**, L041110 (2025).

[5] Zeidler, S. Numerical Tool for Calculating Birefringence in Mirror-Substrates for Gravitational-Wave Detectors. *Frontiers in Astronomy and Space Sciences* **9**, 881348 (2022).

[6] Xu, A.L. et al. Recent progress in structural design strategies of high-birefringence optical crystals. *Coordination Chemistry Reviews* **540**, 216775 (2025).

[7] Leng, B.R. et al. Meta-device: advanced manufacturing. *Light: Advanced Manufacturing* **5**, 117-132 (2024).

[8] Ran, J.J. & Meng, Y.C. Broadband high birefringence and single-polarization hollow-core anti-resonant fibers with an elliptical-like core. *Optics Communications* **575**, 131251 (2025).

[9] Song, Y.H. et al. Ferroelectric Nematic Liquid Crystals Showing High Birefringence. *Advanced Science* **12**, 2414317 (2025).

[10] Zhang, J.R. et al. Multidimensional multiplexing geometric phase metaholography. *Light: Advanced Manufacturing* **6**, 474-485 (2025).

[11] Wei, S. et al. Research Progress of Stress Measurement Technologies for Optical Elements. *International Journal of Optics* **2021**, 5541358 (2021).

[12] De Boer, J.F., Hitzenberger, C.K. & Yasuno, Y. Polarization sensitive optical coherence tomography – a review [Invited]. *Biomedical Optics Express* **8**, 1838-1873 (2017).

[13] Quan, H.D., Shi, W.Q. & Kong, L.B. Non-destructive optical measurement of transparent objects: a review. *Light: Advanced Manufacturing* **6**, 333-357 (2025).

[14] Wang, D.S. et al. Progress and prospect of biomimetic optical materials: a review. *Biogeotechnics* **3**, 100167 (2025).

[15] Li, K.W. et al. Stress birefringence measurement using the multi-harmonic terms of dual cascade photoelastic modulation. *Journal of Instrumentation* **20**, P03033 (2025).

[16] Tang, P.J. et al. Polarization sensitive optical coherence tomography with single input for imaging depth-resolved collagen organizations. *Light: Science & Applications* **10**, 237 (2021).

[17] Choi, B. et al. Giant Optical Anisotropy in 2D Metal–Organic Chalcogenates. *ACS Nano* **18**, 25489-25498 (2024).

[18] Song, S. et al. Polarization-sensitive intensity diffraction tomography. *Light-Science & Applications* **12**, 124 (2023).

[19] Guo, J. et al. Recent progress of residual stress measurement methods: A review. *Chinese Journal of Aeronautics* **34**, 54-78 (2021).

[20] Huang, X.F., Liu, Z.W. & Xie, H.M. Recent progress in residual stress measurement techniques. *Acta Mechanica Solida Sinica* **26**, 570-583 (2013).

[21] Bain, A.K. Crystal Optics: Properties and Applications (Edgbaston: John Wiley & Sons, Inc. 2019).

[22] Saleh, B.E. & Teich, M.C. Fundamentals of photonics (Hoboken: John Wiley & sons, Inc., 2019).

[23] Kaminsky, W., Claborn, K. & Kahr, B. Polarimetric imaging of crystals. *Chemical Society Reviews* **33**, 514-525 (2004).

[24] Dorrah, A.H. & Capasso, F. Tunable structured light with flat optics. *Science* **376**, eabi6860 (2022).

[25] Doualle, T. et al. Laser-induced birefringence measurements by quantitative polarized-phase microscopy. *Optics Letters* **42**, 1616-1619 (2017).

[26] Wang, B.L., Hinds, E. & Krivoy, E. Basic optical properties of the photoelastic modulator part II: residual birefringence in the optical element. Proceedings of SPIE 7461, Polarization Science and Remote Sensing IV. San Diego: SPIE, 2009.

[27] Cranston, E.D. & Gray, D.G. Birefringence in spin-coated films containing cellulose nanocrystals. *Colloids and Surfaces a-Physicochemical and Engineering Aspects* **325**, 44-51 (2008).

[28] Lim, Y. et al. Birefringence measurement of cornea and anterior segment by office-based polarization-sensitive optical coherence tomography. *Biomedical Optics Express* **2**, 2392-2402 (2011).

[29] Arbabi, A. et al. Dielectric metasurfaces for complete control of phase and polarization with subwavelength spatial resolution and high transmission. *Nature nanotechnology* **10**, 937-943 (2015).

[30] Lai, F.X. et al. Nonlinear chiral light generation from resonant metasurfaces. *Nature Communications* **16**, 10686 (2025).

[31] Shi, Z.J. et al. Continuous angle-tunable birefringence with freeform metasurfaces for arbitrary polarization conversion. *Science advances* **6**, eaba3367 (2020).

[32] Dorrah, A.H. et al. Free-standing bilayer metasurfaces in the visible. *Nature Communications* **16**, 3126 (2025).

[33] Kim, S. et al. Anti-aliased metasurfaces beyond the Nyquist limit. *Nature Communications* **16**, 411 (2025).

[34] Aigner, A. et al. Continuous spectral and coupling-strength encoding with dual-gradient metasurfaces. *Nature Nanotechnology* **19**, 1804-1812 (2024).

[35] Yao, C.Y. et al. Data-driven optical method for full-field stress measurements.

Optics Letters **48**, 3091-3094 (2023).

[36] Wang, B.L. & List, J. Basic optical properties of the photoelastic modulator part I: useful aperture and acceptance angle. Proceedings of SPIE 5888, Polarization Science and Remote Sensing II. San Diego: SPIE, 2005.

[37] Wang, S. et al. Dispersion of the Retardation of a Photoelastic Modulator. *Applied Sciences* **9**, 341 (2019).

[38] Kim, I. & Demkov, A.A. Linear electro-optic effect in trigonal LiNbO3: A first-principles study. *Physical Review Materials* **8**, 025202 (2024).

[39] Li, Y. et al. Towards High-Performance Pockels Effect-Based Modulators: Review and Projections. *Micromachines* **15**, 865 (2024).

[40] Kityk, A.V. et al. Dynamic Kerr and Pockels electro-optics of liquid crystals in nanopores for active photonic metamaterials. *Nanoscale* **13**, 18714-18725 (2021).

[41] Ignatyeva, D.O. et al. Birefringence-Mediated Enhancement of the Magneto-Optical Activity in Anisotropic Magnetic Crystals. *Acs Photonics* **9**, 2767-2773 (2022).

[42] Deng, S.W. & Shen, H. Influence of acousto-optic frequency shifter's thermal-induced birefringence on laser frequency-shifted feedback system. *Optics and Lasers in Engineering* **160**, 107290 (2023).

[43] Tokumi, K. et al. Three-dimensional shear stress measurement of stress waves in silica glass induced by a femtosecond laser. *Optics Letters* **50**, 2522-2525 (2025).

[44] Ou, M.Y. et al. Composite achromatic quartz wave plate with adjustable retardation and temperature insensitivity. *Applied Optics* **60**, 6665-6670 (2021).

[45] Zhang, J., Ma, L. & Gong, Y.D. Design and analysis of terahertz trilayer achromatic grating metasurface wave plate. *Scientific Reports* **15**, 5471 (2025).

[46] Steininger, E., Mieling, T. & Chruściel, P.T. Elastically induced phase-shift and birefringence in optical fibers. *Open Research Europe* **5**, 99 (2025).

[47] Nayak, S. et al. Dynamic evolution of internal stress, grain growth, and crystallographic texture in arc-evaporated AlTiN thin films using in-situ synchrotron x-ray diffraction. *Acta Materialia* **272**, 119899 (2024).

[48] Xiao, S., Li, B. & Wang, J. Residual stress birefringence of highly reflective mirrors with different numbers of layers. *Applied Optics* **59**, A99-A105 (2020).

[49] Wang, L.F., Hu, Y.W. & Xue, C.X. Stress analysis of a large diameter aspheric plastic lens in the variable temperature assisted injection molding process. *Applied Optics* **63**, 1320-1329 (2024).

[50] Gao, G.X. et al. Polarization-sensitive digital speckle pattern interferometry for full-field birefringence measurement of biological tissues. *Optics & Laser Technology* **188**, 112941 (2025).

[51] Wang, S. et al. Arbitrary polarization conversion dichroism metasurfaces for all-in-one full Poincaré sphere polarizers. *Light: Science & Applications* **10**, 24 (2021).

[52] Yang, Y.Q., Forbes, A. & Cao, L.C. A review of liquid crystal spatial light modulators: devices and applications. *Opto-Electronic Science* **2**, 230026 (2023).

[53] Yu, P., Li, J.X. & Liu, N. Electrically Tunable Optical Metasurfaces for Dynamic Polarization Conversion. *Nano Letters* **21**, 6690-6695 (2021).

[54] Cannon, T.M. et al. Measuring collagen injury depth for burn severity determination using polarization sensitive optical coherence tomography. *Scientific Reports* **12**, 10479 (2022).

[55] Leica. light-microscopes. at https://www.leica-microsystems.com.cn/cn/.

[56] Nikon. Polarizing Microscopes. at https://www.microscope.healthcare.nikon.com/.

[57] Wang, W. & Chen, J.Z. Simple method for simultaneous determination of the phase retardation and fast axis of a wave plate. *Optik* **124**, 4359-4363 (2013).

[58] Wei, W. et al. Two-Intensity Measurement Method for Determining the Fast Axis and Phase Retardation of a Wave Plate. 2012 Symposium on Photonics and Optoelectronics. IEEE, 2012.

[59] Minzioni, P. et al. Wide-band single-shot measurement of refractive indices and birefringence of transparent materials. *Optics & Laser Technology* **50**, 71-77 (2013).

[60] Cao, Y.H. et al. Measurement of Complex DC Kerr Coefficient of Chalcogenide Glasses by Electric Birefringence. *IEEE Photonics Technology Letters* **36**, 251-253 (2024).

[61] Lapray, P.-J. & Bigué, L. Performance comparison of division of time and division of focal plane polarimeters. Proceedings of SPIE 12749, Sixteenth International Conference on Quality Control by Artificial Vision. Albi: SPIE, 2023.

[62] Ma, F.Y. et al. Instrument-matrix based full-Stokes parameter direct retrieval for snapshot imaging polarimeter. *Optics Express* **33**, 51640-51656 (2025).

[63] del Río-Lima, A. et al. Homemade open-source full-Stokes polarimeter based on division of amplitude. *Applied Optics* **63**, 7177-7187 (2024).

[64] Li, F.-J. et al. Meta-grating-lens–based monolithic polarization camera. *Science Advances* **11**, eadx9886 (2025).

[65] Li, L.W. et al. Flat, wide field-of-view imaging polarimeter. *Optica* **12**, 799-811 (2025).

[66] Bian, S.B. & Arteaga, O. A simple pathway for complete polarization vision. *Scientific Reports* **15**, 8885 (2025).

[67] Ma, Z.B. et al. Study on polarization accuracy and its influencing mechanisms of division of focal plane polarimeter. *Applied Physics B* **131**, 83 (2025).

[68] Wu, X.G. et al. Wavelength-insensitive snapshot Stokes polarimetric imaging based on cascaded metasurfaces. *Advanced Photonics* **7**, 016008 (2025).

[69] Lane, C., Rode, D. & Roesgen, T. Two-dimensional birefringence measurement technique using a polarization camera. *Applied Optics* **60**, 8435-8444 (2021).

[70] Wang, T., Wang, N. & He, S.L. Fast complete Mueller matrix polarimetry microscopy using a single polarization camera. *Optics and Lasers in Engineering* **184**, 108650 (2025).

[71] Ye, M. et al. Polarized imaging characteristics of the twisted nematic liquid-crystal structure leading to an electrically regulated polarimetric camera prototype. *Journal of Optics* **27**, 075701 (2025).

[72] Belle, S., Kefer, S. & Hellmann, R. Spatially Resolved, Real-Time Polarization Measurement Using Artificial Birefringent Metallic Elements. *Photonics* **11**, 397 (2024).

[73] Fan, Q.B. et al. Disordered metasurface enabled single-shot full-Stokes polarization imaging leveraging weak dichroism. *Nature Communications* **14**, 7180 (2023).

[74] Zuo, J.W. et al. Chip-integrated metasurface full-Stokes polarimetric imaging sensor. *Light: Science & Applications* **12**, 218 (2023).

[75] Gao, Y.R. et al. High performance polarization-resolved photodetectors based on intrinsically stretchable organic semiconductors. *Advanced Science* **10**, 2204727 (2023).

[76] Luo, X.H. et al. Intrinsic polarization-sensitive organic photodetector with self-assembled all-polymer heterojunction. *Applied Physics Letters* **121**, 233301 (2022).

[77] Chen, Q.L. et al. Manipulating perovskite structural asymmetry for high-performing self-powered full-stokes polarimetry. *Science Advances* **11**, eads6123 (2025).

[78] Su, M. et al. Boosting Chirality Transfer in Chiral Perovskites via Structural Asymmetry Regulation Enables High-Performance Self-Driven Full-Stokes Polarimetry. *Small Methods* **10**, e02219 (2026).

[79] Liu, X.S. et al. Metaphotonic photodetectors for direct Stokes quantification. *Nature Electronics* **8**, 1099-1107 (2025).

[80] Panda, J. et al. Polarization-resolved position-sensitive self-powered binary photodetection in multilayer janus CrSBr. *ACS Applied Materials & Interfaces* **16**, 1033-1043 (2024).

[81] Zhu, X.Y. et al. One-shot measurement of birefringence by radial analysis. *Measurement* **235**, 114941 (2024).

[82] Lo, Y.L. et al. Simultaneous absolute measurements of principal angle and phase retardation with a new common-path heterodyne interferometer. *Applied Optics* **43**, 2013-2022 (2004).

[83] Li, C.Y. Study of high-precision glass stress testing technology. Xi'an Institute of Optics & Precision Mechnics, Chinese Academy of Science. 2014.

[84] Li, K.W. et al. Fast and full range measurements of ellipsometric parameters using a 45° dual-drive symmetric photoelastic modulator. *Optics Express* **25**, 5725-5733 (2017).

[85] Wu, X.Y. et al. High-speed polarized light microscopy for in situ, dynamic measurement of birefringence properties. *Measurement Science and Technology* **29**, 015203 (2018).

[86] Prętka, M. et al. Evaluation of a linear birefringence measurement method with

increased sensitivity. *Applied Optics* **55**, 868-872 (2016).

[87] Lin, S.T. et al. Heterodyne polariscope for measuring the principal angle and phase retardation of stressed plastic substrates. *Measurement* **175**, 109096 (2021).

[88] Chen, K.H. et al. Alternative method for measuring the phase retardation and fast axis of a wave plate. *Optical Review* **26**, 652-658 (2019).

[89] Li, K.W., Wang, S. & Wang, Z.B. Measurement of Waveplate Parameters over Entire Clear Aperture Based on Differential Frequency Modulation with Dual Photoelastic Modulators. *Applied Sciences* **13**, 4496 (2023).

[90] Tong, H. et al. Calibration of elliptical retarders in Mueller matrix spectroscopic polarimetry and ellipsometry. *Optics Express* **33**, 28277-28289 (2025).

[91] Yu, X.T. et al. Rapid Mueller Matrix Holographic Microscopy Imaging for Polarization Sensitive Materials. *IEEE Transactions on Instrumentation and Measurement* **74**, 4511711 (2025).

[92] Feng, Y.H. et al. Ultrafast polarization characterization with Mueller matrix based on optical time-stretch and spectral encoding. *Optics Express* **32**, 9128-9138 (2024).

[93] Oh, J. et al. Ultra-wide-field imaging Mueller matrix spectroscopic ellipsometry for semiconductor metrology. *Nature Communications* **16**, 8512 (2025).

[94] Zaidi, A. et al. Metasurface-enabled single-shot and complete Mueller matrix imaging. *Nature Photonics* **18**, 704-712 (2024).

[95] Fells, J.A.J. et al. Time-resolved retardance and optic-axis angle measurement system for characterization of flexoelectro-optic liquid crystal and other birefringent devices. *Optics Express* **26**, 6126-6142 (2018).

[96] Twu, R.C. & Chu, Y.F. Measurements of photorefractive birefringence on the different propagation directions in electro-optic crystals. *Measurement* **121**, 1-5 (2018).

[97] Zhang, R., Chen, Y. & Jing, N. High-precision measurement of mid-infrared waveplate phase retardation based on dual photoelastic difference frequency modulation. *Acta Optica Sinica* **39**, 0312002 (2019).

[98] Del Hoyo, J. et al. Interferometric method for simultaneous characterization of retardance and fast axis of a retarder. *Optics and Lasers in Engineering* **179**, 108262 (2024).

[99] Muñoz, J.D. et al. Interferometric method for characterizing optical retarders. Proceedings of SPIE 12997, Optics and Photonics for Advanced Dimensional Metrology III. Strasbourg: SPIE, 2024.

[100] Baumann, B. Polarization Sensitive Optical Coherence Tomography: A Review of Technology and Applications. *Applied Sciences* **7**, 474 (2017).

[101] Jones, G.L. et al. Single-input polarization-sensitive optical coherence tomography through a catheter. *Biomedical Optics Express* **14**, 4609-4626 (2023).

[102] Kahatapitiya, N.S. et al. Optical Coherence Tomography for High-Precision Industrial Inspection in Industry 4.0: Advances, Challenges, and Future Trends. *Laser & Photonics Reviews*, e02290 (2025).

[103] Yang, D. et al. Compact spectral-polarization-modulation method for rapid and versatile polarization measurements in interferometric imaging. *Photonics Research* **13**, 1049-1059 (2025).

[104] Lang, K.C. & Teng, H.K. Interferometric measurement of temporal behavior of linear birefringence with extended range. *Applied Optics* **56**, 7718-7725 (2017).

[105] Wei, S. et al. Laser heterodyne based stress measurement technology for optical elements. *Infrared Physics & Technology* **119**, 103969 (2021).

[106] Schnoor, N.P. et al. Calibration of liquid crystal variable retarders using a common-path interferometer and fit of a closed-form expression for the retardance curve. *Applied Optics* **59**, 10673-10679 (2020).

[107] Cheng, L. et al. Sagnac Interferometric Temperature Sensor Based on Boron-Doped Polarization-Maintaining Photonic Crystal Fibers. *Optics* **3**, 400-408 (2022).

[108] Khan, S.N., Chatterjee, S.K. & Chaudhuri, P.R. Single all-optical platform for measurement of twist and transverse stress using polarization modulation in distinct dual-mode fiber placed in a Sagnac loop. *Journal of the Optical Society of America A-Optics, Image Science, and Vision* **33**, 131-140 (2016).

[109] Tan, M. et al. Fast and high-resolution polarization error test of large aperture optics using polarization-tunable interferometric methods. *Optics Express* **33**, 5108-5122 (2025).

[110] Xu, X. et al. High Sensitivity and Full-Circle Optical Rotary Sensor for Non-Cooperatively Tracing Wrist Tremor With Nanoradian Resolution. *IEEE Transactions on Industrial Electronics* **69**, 9605-9612 (2022).

[111] Zhang, L. et al. Two-dimensional flow vector measurement based on all-fiber laser feedback frequency-shifted multiplexing technology. *Photonics Research* **12**, 1371-1378 (2024).

[112] Zhao, Y.Y. et al. Coherent laser detection of the femtowatt-level frequency-shifted optical feedback based on a DFB fiber laser. *Optics Letters* **46**, 1229-1232 (2021).

[113] Tan, Y.D., Zhang, S.L. & Zhang, Y.N. Laser feedback interferometry based on phase difference of orthogonally polarized lights in external birefringence cavity. *Optics Express* **17**, 13939-13945 (2009).

[114] Chen, W.X. et al. Polarization flipping and hysteresis phenomenon in laser with optical feedback. *Optics Express* **21**, 1240-1246 (2013).

[115] Deng, S.W. et al. Amplitude and phase modulation of optical feedback in a-cut Nd:YVO_4 laser with a birefringent external cavity. *Laser Physics Letters* **19**, 095002 (2022).

[116] Deng, S.W. et al. Frequency-shifted dynamics of Nd:YVO_4 laser with anisotropic and quite weak optical feedback. *Results in Physics* **43**, 106104 (2022).

[117] Nechay, K. et al. AlGaAs/AlGaInP VECSELs With Direct Emission at 740–770 nm. *IEEE Photonics Technology Letters* **31**, 1245-1248 (2019).

[118] Tang, N. et al. Intensity modulation of orthogonally polarized laser with two

weak light reinjection beams of the bifurcated sub-cavity. *Applied Optics* **63**, 5951-5955 (2024).

[119] Zhang, P. et al. Measurement method for optical retardation based on the phase difference effect of laser feedback fringes. *Applied Optics* **54**, 204-209 (2015).

[120] Niu, H.S., Niu, Y.X. & Li, J.Y. Measurement of stress-induced birefringence in glasses based on reflective laser feedback effect. *Optical Engineering* **56**, 024104 (2017).

[121] Deng, S.W. et al. Highly Sensitive Self-calibrating Birefringence Measurement Based on Anisotropic Laser Feedback Polarization Effect. *PhotoniX* **6**, 49 (2025).

[122] Wu, Y. Birefringence /Polarized optica Feedback in HeNe aser and lts Displacement Measurement System. Tsinghua University. 2014.

[123] Coppola, G. & Ferrara, M.A. Polarization-sensitive digital holographic imaging for characterization of microscopic samples: Recent advances and perspectives. *Applied Sciences* **10**, 4520 (2020).

[124] Li, G.Q. et al. Single-Shot high Bandwidth-Utilization Jones matrix measurement based on Kramers–Kronig holographic multiplexing. *Optics & Laser Technology* **192**, 113915 (2025).

[125] Qiu, Y.P. et al. Resolution-enhanced real-time Jones matrix measuring via Kramers-Kronig relations. *Optics Express* **33**, 18346-18357 (2025).

[126] Liu, H.C. et al. Common-path polarization holography with partial coherent illumination for single-shot Jones matrix measurement. *Optics Letters* **50**, 6694-6697 (2025).

[127] Liu, H.Z. et al. Real-Time Jones Matrix Synthesis by Compact Polarization Inline Holographic Microscopy. *Laser & Photonics Reviews* **18**, 2301261 (2024).

[128] Chen, K. et al. Stress measurement based on 1556 nm fiber laser frequency splitting effect. *Acta Physica Sinica* **68**, 104201 (2019).

[129] She, K. et al. Rapid measurement method of intracavity phase retardation based on laser frequency splitting. *Optics Express* **31**, 35032-35040 (2023).

[130] Gong, M. et al. Ptychographic Mueller matrix imaging (PMMI): principle and proof-of-concept demonstration. *Optics Letters* **49**, 6409-6412 (2024).

[131] Gong, M. et al. Ptychographic Mueller matrix imaging: in-situ system calibration and evaluation. *Optics Letters* **50**, 6137-6140 (2025).

[132] Bei, C., Zhang, X.J. & Zhu, J.Q. Measurement of a birefringent sample based on ptychographical iterative engine using planar polariscope. *Journal of Physics D-Applied Physics* **53**, 05LT01 (2020).

[133] Park, K. et al. Jones matrix microscopy for living eukaryotic cells. *ACS Photonics* **8**, 3042-3050 (2021).

[134] Dai, X. et al. Quantitative Jones matrix imaging using vectorial Fourier ptychography. *Biomedical optics express* **13**, 1457-1470 (2022).

[135] Gao, W.X. et al. Polarization imaging for residual stress analysis in optically transparent materials: a review. *Optics & Laser Technology* **192**, 113642 (2025).

[136] Li, Z.Q. et al. Full-field measurement of residual stress in single-crystal diamond

substrates based on Mueller matrix microscopy. *Measurement* **234**, 114790 (2024).

[137] Kovács, Z. et al. Quantitative shear stress imaging in high throughput in-line Si wafer inspection. *Materials Science in Semiconductor Processing* **178**, 108449 (2024).

[138] Vargas-Isaza, C., Posada-Correa, J. & Briñez-De León, J. Analysis of the Stress Field in Photoelasticity Used to Evaluate the Residual Stresses of a Plastic Injection-Molded Part. *Polymers* **15**, 3377 (2023).

[139] Wang, J. et al. Qualitative characterization of residual stress of injection molded polycarbonate goggles based on photoelasticity and digital image processing technique. *Frontiers in Materials* **10**, 1242721 (2023).

[140] Parkinson, J. et al. Mueller polarimetry for quantifying the stress optic coefficient in the infrared. *Optical Engineering* **63**, 094104 (2024).

[141] Terakado, N. et al. A novel method for stress evaluation in chemically strengthened glass based on micro-Raman spectroscopy. *Communications Physics* **3**, 37 (2020).

[142] Jagailloux, F. et al. Applied Photoelasticity for Residual Stress Measurement inside Crystal Silicon Wafers for Solar Applications. *Strain* **52**, 355-368 (2016).

[143] Gao, G.H. et al. Investigation of Photoelastic Property and Stress Analysis for Optical Polyimide Membrane through Stress Birefringence Method. *Coatings* **10**, 56 (2020).

[144] Zeidler, S. et al. Correlation between birefringence and absorption mapping in large-size Sapphire substrates for gravitational-wave interferometry. *Scientific Reports* **13**, 21393 (2023).

[145] Feng, X.W. et al. Visualizing the Shear Flow-Modulated Alignments in Cellulose Nanocrystal Films by the Mueller Matrix. *The Journal of Physical Chemistry C* **127**, 6974-6980 (2023).

[146] Wang, Y.H. et al. Visualizing the Electric Field-Modulated Cellulose Nanocrystal Films by Mueller Matrix Microscopy. *ACS Applied Materials & Interfaces* **17**, 55263-55273 (2025).

[147] Feng, Y.Z. et al. Visible to mid-infrared giant in-plane optical anisotropy in ternary van der Waals crystals. *Nature Communications* **14**, 6739 (2023).

[148] Oldenbourg, R. Polarized light field microscopy: an analytical method using a microlens array to simultaneously capture both conoscopic and orthoscopic views of birefringent objects. *Journal of Microscopy* **231**, 419-432 (2008).

[149] Ge, B.L. et al. Single-Shot Quantitative Polarization Imaging of Complex Birefringent Structure Dynamics. *Acs Photonics* **8**, 3440-3447 (2021).

[150] Zhang, M.S. et al. $HgBr_2$: an easily growing wide-spectrum birefringent crystal. *Chemical Science* **15**, 6891-6896 (2024).

[151] Slavich, A.S. et al. Exploring van der Waals materials with high anisotropy: geometrical and optical approaches. *Light: Science & Applications* **13**, 68 (2024).

[152] Mei, H.Y. et al. Colossal Optical Anisotropy from Atomic-Scale Modulations.

Advanced Materials **35**, 2303588 (2023).

[153] Bouhy, J. et al. Unsupervised topological analysis of polarized light microscopy: application to quantitative birefringence imaging. *Applied Optics* **63**, 1188-1195 (2024).

[154] Cao, L.L. et al. A microcrystal method for the measurement of birefringence. *Crystengcomm* **22**, 1956-1961 (2020).

[155] Lad, J. et al. Polarimetric biomarkers of peri-tumoral stroma can correlate with 5-year survival in patients with left-sided colorectal cancer. *Scientific Reports* **12**, 12652 (2022).

[156] Liu, X.Y. et al. Posterior scleral birefringence measured by triple-input polarization-sensitive imaging as a biomarker of myopia progression. *Nature Biomedical Engineering* **7**, 986-1000 (2023).

[157] Keikhosravi, A. et al. Real-time polarization microscopy of fibrillar collagen in histopathology. *Scientific Reports* **11**, 19063 (2021).

[158] Majumdar, A. et al. Machine learning based local recurrence prediction in colorectal cancer using polarized light imaging. *Journal of Biomedical Optics* **29**, 052915 (2023).

[159] Yashin, K.S. et al. Quantitative nontumorous and tumorous human brain tissue assessment using microstructural co- and cross-polarized optical coherence tomography. *Scientific Reports* **9**, 2024 (2019).

[160] Tumanova, K. et al. Mueller matrix polarization parameters correlate with local recurrence in patients with stage III colorectal cancer. *Scientific Reports* **13**, 13424 (2023).

[161] Bouchal, P. et al. High-Resolution Quantitative Phase Imaging of Plasmonic Metasurfaces with Sensitivity down to a Single Nanoantenna. *Nano Letters* **19**, 1242-1250 (2019).

[162] Nacius, E. et al. Focal zone engineering with hollow spatially variable waveplates applicable in laser micromachining. *Procedia CIRP* **111**, 609-612 (2022).

[163] Zuo, J.W. et al. Metasurface-Based Mueller Matrix Microscope. *Advanced Functional Materials* **34**, 2405412 (2024).

[164] Rothe, S. et al. Securing Data in Multimode Fibers by Exploiting Mode-Dependent Light Propagation Effects. *Research* **6**, 0065 (2023).

[165] Deng, Y.D. et al. Recent progress in metasurface-enabled optical waveplates. *Nanophotonics* **11**, 2219-2244 (2022).

[166] Zhang, L. & Cui, T.J. Space-Time-Coding Digital Metasurfaces: Principles and Applications. *Research* **2021**, 9802673 (2021).

[167] Hua, Y.K. et al. A Fast and Simultaneous Method for Measuring Wave Plate PhaseRetardation and Fast Axis Azimuth. *Laser & Optoelectronics Progress* **55**, 021202 (2018).

[168] Chen M. et al. High-precision electro-optic modulated ellipsometric stress sensing system. *Chinese Optics* **18**, 691-697 (2025).

[169] Lang, K.C. & Teng, H.K. Time resolved retardation and orientation measurement

by common path heterodyne interferometer. *Optics Communications* **440**, 61-67 (2019).

[170] Zhang, P. et al. Methods for optical phase retardation measurement: a review. *Science China Technological Sciences* **56**, 1155-1164 (2013).

[171] Kim, J. et al. Ptychographic lens-less birefringence microscopy using a mask-modulated polarization image sensor. *Scientific reports* **13**, 19263 (2023).

[172] Chen, W.L. et al. Extended eigenvalue calibration method for Mueller matrix polarimetry with four photoelastic modulators. *Optics Letters* **50**, 840-843 (2025).

[173] Zhang, J. et al. Self-calibration for a spatially modulated snapshot Mueller matrix imaging polarimeter. *Applied Optics* **64**, 7968-7975 (2025).

[174] Wang, Y.S. et al. Realization of ultra-small stress birefringence detection with weak-value amplification technique. *Applied Physics Letters* **118**, 161104 (2021).

[175] Guan, C.Z. et al. Calibration strategies for dual-angle Mueller matrix polarimetry using individual microsphere. *Measurement* **255**, 117908 (2025).

[176] Huang, T.Y. et al. Hybrid calibration method for Mueller matrix microscopy. *Optics and Lasers in Engineering* **165**, 107543 (2023).

[177] Zhang, X.L. et al. Precise detection of tiny birefringence with accuracy reaching 10^{-11} level. *Nature Communications* **16**, 6434 (2025).

[178] Yang, H. et al. Optical Waveplates Based on Birefringence of Anisotropic Two-Dimensional Layered Materials. *Acs Photonics* **4**, 3023-3030 (2017).

[179] Jin, M. et al. 1/f-noise-free optical sensing with an integrated heterodyne interferometer. *Nature Communications* **12**, 1973 (2021).

[180] Bian, L.H. et al. A broadband hyperspectral image sensor with high spatio-temporal resolution. *Nature* **635**, 73-81 (2024).

[181] Ma, J.Y. et al. Integrated diffractive full-Stokes spectro-polarimetric imaging. *Optics Express* **33**, 51223-51236 (2025).

[182] Lopera, M.J. et al. Mueller-Gabor holographic microscopy. *Optics and Lasers in Engineering* **178**, 108191 (2024).

[183] Gutiérrez, Y. et al. Subpicosecond spectroscopic ellipsometry of the photoinduced phase transition in VO2 thin films. *ACS photonics* **11**, 4883-4893 (2024).

[184] Herrfurth, O. et al. Transient birefringence and dichroism in ZnO studied with fs-time-resolved spectroscopic ellipsometry. *Physical Review Research* **3**, 013246 (2021).

[185] Bao, Y.J. & Li, B.J. Single-shot simultaneous intensity, phase and polarization imaging with metasurface. *National Science Review* **12**, nwae418 (2025).

[186] Ge, B.L. et al. Single-Shot Optical Anisotropy Imaging with Quantitative Polarization Interference Microscopy. *Laser & photonics reviews* **12**, 1800070 (2018).

[187] Shan, M.G. et al. Compact common-path polarization holography for measurement of the Jones matrix of polarization-sensitive materials. *Optics Express* **32**, 30065-30075 (2024).

---

[188] Gulo, D.P. et al. Exploring optical properties of 2 H-and 1 T′-MoTe 2 single crystals by spectroscopic ellipsometry. *Physical Review Materials* **7**, 044001 (2023).

[189]Wen, S. et al. Metasurface array for single-shot spectroscopic ellipsometry. *Light: Science & Applications* **13**, 88 (2024).

[190] Kopf, L., Barros, R. & Fickler, R. Correlating space, wavelength, and polarization of light: Spatiospectral vector beams. *ACS Photonics* **11**, 241-246 (2023).

[191] Yang, K. et al. Data-driven polarimetric imaging: a review. *Opto-Electronic Science* **3**, 230042 (2024).

[192] Gao, W.R. Mueller matrix decomposition methods for tissue polarization tomography. *Optics and Lasers in Engineering* **147**, 106735 (2021).

[193] Qiu, Y.P. et al. Single-shot measurement of the Jones matrix for anisotropic media using four-channel digital polarization holography. *Applied Optics* **62**, 7890-7894 (2023).

[194] Ma, X. et al. Fast and high-accuracy collinear reflection Mueller imaging polarimeter implemented with the compound calibration method. *Applied Optics* **63**, 3381-3389 (2024).

[195] Zuo, C. et al. Deep learning in optical metrology: a review. *Light: Science & Applications* **11**, 39 (2022).

[196] Shi, H.D. et al. Deep learning for polarization optical system automated design. *Photonics* **11**, 164 (2024).

[197] Zeng, Y.H. et al. From performance to structure: a comprehensive survey of advanced metasurface design for next-generation imaging. *npj Nanophotonics* **2**, 39 (2025).

[198] Li, X.B. et al. Polarimetric imaging via deep learning: A review. *Remote Sensing* **15**, 1540 (2023).

[199] Weng, J.Y., Gao, C. & Lei, B. Real-time polarization measurement based on spatially modulated polarimeter and deep learning. *Results in Physics* **46**, 106280 (2023).

[200] Hu, H.F. et al. Physics-informed neural network for polarimetric underwater imaging. *Optics Express* **30**, 22512-22522 (2022).

[201] Pan, M.N. et al. Feasibility of deep learning-based polarization-sensitive optical coherence tomography angiography for imaging cutaneous microvasculature. *Biomedical Optics Express* **14**, 3856-3870 (2023).

[202] Jung, J. et al. Neural network-based analysis algorithm on Mueller matrix data of spectroscopic ellipsometry for the structure evaluation of nanogratings with various optical constants. *Nanophotonics* **14**, 471-484 (2025).

[203] Wei, H.Y. et al. Deep Learning Tongue Cancer Detection Method Based on Mueller Matrix Microscopy Imaging. *Optics* **6**, 35 (2025).

[204] Tahara, T. & Shimobaba, T. High-speed phase-shifting incoherent digital holography (invited). *Applied Physics B* **129**, 96 (2023).

[205] Shen, Z.C. et al. Monocular metasurface camera for passive single-shot 4D imaging. *Nature Communications* **14**, 1035 (2023).

[206] Fu, B.Y. et al. Miniaturized high-efficiency snapshot polarimetric stereoscopic imaging. *Optica* **12**, 391-398 (2025).